Recent progress in scanning electron microscopy for the characterization of fine structural details of nano materials

Mitsuo Suga [a,*], Shunsuke Asahina [a], Yusuke Sakuda [a], Hiroyoshi Kazumori [a], Hidetoshi Nishiyama [a], Takeshi Nokuo [a], Viveka Alfredsson [b], Tomas Kjellman [b], Sam M. Stevens [c], Hae Sung Cho [d], Minhyung Cho [d], Lu Han [e], Shunai Che [e], Michael W. Anderson [f], Ferdi Schüth [g], Hexiang Deng [h], Omar M. Yaghi [i], Zheng Liu [j], Hu Young Jeong [k], Andreas Stein [l], Kazuyuki Sakamoto [m], Ryong Ryoo [n,o], Osamu Terasaki [d,p,**]

[a] JEOL Ltd., SM Business Unit, Tokyo, Japan
[b] Physical Chemistry, Lund University, Sweden
[c] Private Contributor, UK
[d] Graduate School of EEWS, KAIST, Republic of Korea
[e] School of Chemistry & Chemical Engineering, Shanghai Jiao Tong University, China
[f] Centre for Nanoporous Materials, School of Chemistry, University of Manchester, UK
[g] Department of Heterogeneous Catalysis, Max-Planck-Institut für Kohlenforschung, Mülheim, Germany
[h] College of Chemistry and Molecular Sciences, Wuhan University, China
[i] Department of Chemistry, University of California, Berkeley, USA
[j] Nanotube Research Center, AIST, Tsukuba, Japan
[k] UNIST Central Research Facilities/School of Mechanical & Advanced Materials Engineering, UNIST, Republic of Korea
[l] Department of Chemistry, University of Minnesota, Minneapolis, USA
[m] Department of Nanomaterials Science, Chiba University, Japan
[n] Centre for Nanomaterials & Chemical Reactions, IBS, Republic of Korea
[o] Department of Chemistry, KAIST, Republic of Korea
[p] Department of Materials & Environmental Chemistry, Stockholm University, Sweden

Keywords:
Scanning electron microscopy
Through-the-lens detection system
Nano-materials
Atmospheric SEM
Metal-organic frameworks
Mesoporous materials

A B S T R A C T

Research concerning nano-materials (*metal-organic frameworks* (*MOFs*), *zeolites*, *mesoporous silicas*, *etc.*) and the nano-scale, including potential barriers for the particulates to diffusion to/from is of increasing importance to the understanding of the catalytic utility of porous materials when combined with any potential super structures (such as hierarchically porous materials). However, it is difficult to characterize the structure of for example *MOFs* via X-ray powder diffraction because of the serious overlapping of reflections caused by their large unit cells, and it is also difficult to directly observe the opening of surface pores using ordinary methods. Electron-microscopic methods including *high-resolution scanning electron microscopy* (*HRSEM*) have therefore become imperative for the above challenges. Here, we present the theory and practical application of recent advances such as through-the-lens detection systems, which permit a reduced landing energy and the selection of high-resolution, topographically specific emitted electrons, even from electrically insulating nano-materials.

© 2014 Elsevier Ltd. All rights reserved.

Contents

  * Corresponding author.
  ** Corresponding author. Graduate School of EEWS, KAIST, Republic of Korea.
    E-mail addresses: msuga@jeol.co.jp (M. Suga), terasaki@mmk.su.se, terasaki@kaist.ac.kr (O. Terasaki).

1. Introduction

For research concerning *nano-materials*, it is necessary to observe the morphology and composition of samples. At present, scanning electron microscopy (SEM) is heavily used in the pursuit of the further understanding *nano-materials,* because of the recent significant improvements in SEM for imaging, diffraction and elemental analysis in terms of spatial resolution and sensitivities [1,2]. Here, we use the word "*nano-material*" to represent a material that exhibits characteristic features in its physical and chemical properties that have origins in the material's structure at the nanoscopic level. In this review article, recent improvements in SEM and their effect on *nano-material* characterizations and their dependence upon the use of low landing energies are presented.

1.1. The basic principles of SEM

An SEM demagnifies an electron beam that is produced by a source into a probe which scans across the surface of a sample in raster fashion (Fig. 1a). The interaction between the sample and the electron probe (*impacted electrons − IE*) produces various types of *emissions,* which are captured by different detectors placed in appropriate positions.

Morphological/topological-contrast and compositional information are separately obtained by selecting specific types of emitted electrons, known as *secondary electrons* (*SEs* − with energies smaller than 50 eV) and *backscattered electrons* (*BSEs* − with energies larger than 50 eV), respectively; see Fig. 1b. Further compositional information is obtained through the detection of characteristic X-rays using an X-ray detector.

While *transmission electron microscopes* (TEMs) remain the most-used type microscopes for the characterization of crystal defects at the atomic scale, SEMs

1. do not require extensive sample preparation and yet may produce similar results through the detection of *BSEs* with selected angles;
2. retain a much large depth of field (wide observable range in *z*-axis with acceptable resolution) allowing a considerable amount
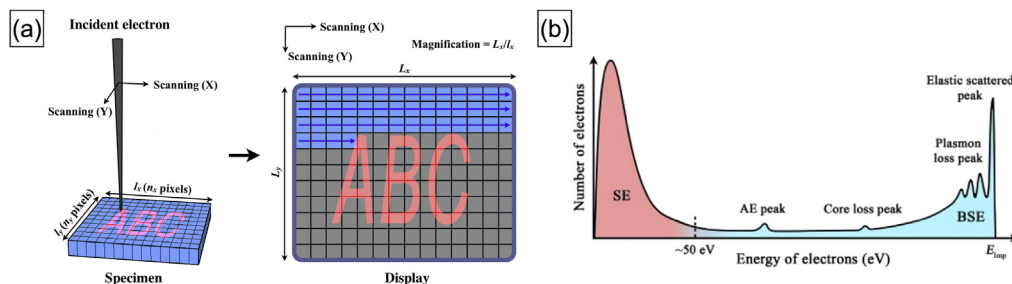
Fig. 1. Basic depictions of (a) the rastering of an electron beam across a sample and the emitted signal is transferred as a function of position on a pixelated image/monitor and (b) the emitted energy spectrum from *secondary electrons* (*SEs*) to elastically reflected electrons.

of large-scale structural data to be collected at reduced magnification (*x*- and *y*-axis) (see Fig. 2);

3. can realize observations of samples in liquid or air under atmospheric pressure, which can be achieved using an electron-beam-transparent film and
4. do not require any mechanical crushing causing destruction of the sample, thus permitting morphological information and surface information to be retained. This last point is of increasing importance because most chemical reactions occur on the surfaces, both external surfaces and those of pore-walls inside a crystal, and the direct confirmation of pores that open to an external surface is crucial for nanoporous materials

Point 2 is discussed here, while all others will be addressed in detail later in this article. A sample of *three-dimensionally ordered macroporous* (*3DOM*) carbon, which was synthesized in Stein's laboratory can be seen to exhibit a very regular arrangement of pores in an *fcc* arrangement [3–5]. Two small regions are digitally expanded in Fig. 2b and c. Despite the height differences between the regions, both display all the important structural details of three types of {111} facets: (111), ($\overline{1}\overline{1}$1) and ($\overline{1}$11) planes.

1.2. Early development of SEM

Electron microscopy (EM) was invented by Ruska and Knoll in 1931 [6,7]. The first electron microscope was a TEM. Four years later, Knoll et al. developed a precursor to modern SEM, in which the sample, instead of the electron probe, was moved and the emitted electrons were detected to form an SEM image [8]. The primary aim of their research was to study the interactions between the electrons and the sample surface, so no focusing mechanism was applied to the electron beam leading to spatial resolutions of approximately 100 μm.

In 1938, von Ardenne used two magnetic lenses, and scan coils to achieve the electromagnetic scanning of a focused electron beam with a diameter of 50–100 nm on a specimen [9,10]. This was the first experiment to detect the signals from a focus electron beam. The lack of effective detectors for *BSEs* and *SEs* at this time meant the equipment was primarily used as a *scanning transmission electron microscope* (STEM), detecting transmitted electrons using photographic film.

Zworykin, Hilier, and Snyder developed two types of SEM based on the use of an *objective lens* to demagnify the electron beam into a probe: magnetic lens and electrostatic lens [11]. The latter achieved a spatial resolution of 50 nm using a retarding-type lens, a *through-the lens* (*TTL*) detector and (unsuccessful because of the poor vacuum technology at that time) a cold field emitter; all three of these technologies are presently used in commercial high-resolution equipment. The detection of signal electrons with low noise was difficult at that time a facsimile printer was used for image recording, the slow speed of which made it commercially unviable.

Oatley's team at Cambridge University developed the physical understanding of SEM [12,13]. Their associated hardware advancements, including the *Everhart-Thornley detector* (*ET detector*), allowed SEM to achieve commercial viability [14]. The improved detector performance achieved using the combination of a
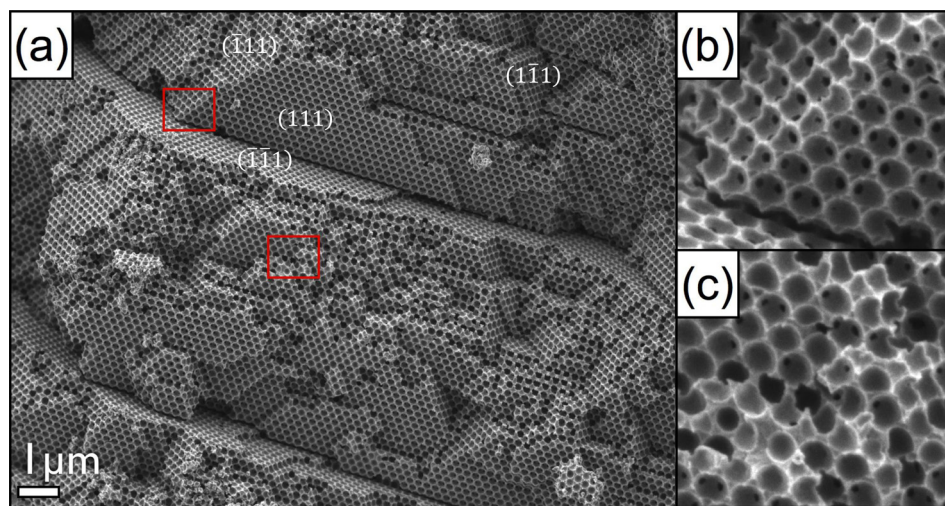
Fig. 2. *High-resolution scanning electron microscopy* (*HRSEM*) image of *3DOM* carbon demonstrating high resolution and depth of field at low magnification. (b) and (c) are digital magnifications of the red boxes in (a) taken at 5120 × 3840 pixels. Conditions: WD = 9.9 mm; Detector = LED; Landing energy = 1 keV; M = 5000×. (For interpretation of the references to color in this figure legend, the reader is referred to the web version of this article.)

fluorescent screen and a photomultiplier permitted real-time capture by displaying the SEM image on a cathode-ray tube (CRT), and the same principle is still used in modern SEM systems. Oatley's team also promoted the use of magnetic objective lenses over the commonly used electrostatic standard of the time for SEMs [12,15], because aberrations in a magnetic lens are smaller, and it is easier to focus a high-energy electron beam using such lenses than using einzel-type electrostatic lenses [12].

1.2.1. Electron source

A thermionic electron source was initially used, and such sources are still used now in cost-effective SEMs [16]. Crewe et al. developed a cold field emitter for EMs [17], where electrons are emitted from a filament through the exploitation of the tunneling effect. Later, an alternative called a Schottky emitter was developed [18,19]. A Schottky emitter is sometimes called as a thermal field emitter because the same hardware is occasionally used as the thermal field emitter [20], though it operates by the principle of Schottky emission, in which thermally excited electrons originate from a bulk material, and the barrier height is reduced by a strong electric field. SEMs equipped with these three types of electron sources are called *FE-SEMs* and produce higher-resolution images because of their smaller spot size.

1.3. Contrast formation

The interaction of the probe with the sample produces various electrons from a depth, *R*, a good approximation for which is given by Equation (1) [20,21], where A = mass number; E_0 = energy of *IE*, ρ = density; and Z = atomic number.

$$R(\text{nm}) \approx \frac{27.6 \cdot A \cdot (\text{g} \cdot \text{mole}^{-1}) \cdot E_0 \cdot (\text{KeV})^{1.67}}{\rho(\text{g} \cdot \text{cm}^{-3}) \cdot Z^{0.889}} \quad (1)$$

SEs originate from the *IE*, *BSEs* escaping from the sample surface, and *BSEs* smashing the sample chamber. *SEs* from these three sources are referred to as *SE1*, *SE2* and *SE3*, respectively (Fig. 3). These different types of emitted electrons produce signals of different resolutions and contrast types [22].

1.3.1. Composition

The direction of *IEs* can vary primarily because of elastic scattering in a sample. A typical model used to explain the *cross-section* of elastic scattering is the screened Rutherford model that is described as follows [23]. (A Mott cross section may be used for more explicit calculations [23,24].)

$$\frac{d\sigma_{\text{el}}}{d\Omega} = |f(\theta)|^2 = \frac{e^4 Z^2}{4(4\pi\varepsilon_0)^2 m^2 v^4} \cdot \frac{1}{\left[\sin^2(\theta/2) + \sin^2(\theta_0/2)\right]^2} \quad (2)$$

$$\sin(\theta_0/2) \simeq \theta_0/2 = \lambda/4\pi R \quad (3)$$

$$R = a_{\text{H}} Z^{-1/3} \quad (4)$$

$$a_{\text{H}} = h^2 \varepsilon_0 / \pi m_0 e^2 \quad (5)$$

here, σ = total elastic cross section, e = charge of an electron, Z = atomic number, ε = dielectric constant, m = mass of an electron, v = velocity of the electron, a_{H} = the Bohr radius = 0.0569 nm, and λ = wavelength of the electron.

Elastically scattered electrons whose trajectories are sufficiently altered may exit through the sample surface as *BSEs*. (They may

Fig. 3. Schematic of the electrons emitted from a range, *R*, below the surface of the sample. Various kinds of electrons are emitted from the sample. *SE1* is generated from *impacted electrons* (*IE*) right after the incidence, which has spatially localized information (σ1). Then, *IE* spread to interaction volume with a size of range *R*. Part of *IEs* are emitted from the surface, and most of them are *BSEs* with maximum escape volume described in the figure. *SE2s* are *SEs* which are generated from *BSEs* when they pass through the surface. *SE3s* are *SEs* generated at a lens or a sample chamber when *BSEs* hit their surfaces. Since *SE2* and *SE3* are from *BSEs*, they have rather spatially broad information (σ23).

have undergone inelastic collisions in the process, however all have an emitted energy, by definition, of greater than 50 eV) Their number is strongly related to the cross section given in Equation (2) and, ultimately, to Z^2. *BSEs* therefore produce compositional contrast.

1.3.2. Orientation

The intensity of *BSEs* also depends on the lattice orientation of a crystalline sample. *IEs* injected along a lattice plane or a zone axis propagate deep into the sample (called *planar* or *axial channeling*) so the amount of BSEs becomes small compared to *IEs* that are not injected along a crystal plane. This fact forms the basis of *electron channeling contrast imaging* (*ECCI*) that will be explained in Section 5.4.

1.3.3. Topography

IEs and *BSEs* that inelastically interact with the sample create *SE1* and *SE2*, respectively. The combination of the much shorter escape depth of *SEs* than *BSEs* (typically <2 nm and approximately 5 nm, respectively, at a 1 keV landing energy [25]) and the fact that SE emission is proportional to sec[θ] (θ = surface tilt) causes the image contrast of these types of the *SEs* to be highly topographic [23].

Superfine structures are further enhanced by the *edge effect* to atomic-level resolution: when the electron probe reaches the edge of a crystal surface or there is a sufficiently large undulation that the interaction volume protrudes outside of the material, extra *SE2s* will be produced. Fig. 4 shows the imaging of terraces on the surface of *Linde type A Zeolite A* (*LTA*). Transference of the sample to an *atomic force microscope* (*AFM*), where the crystals were relocated and imaged *ibidem* (at the same location), confirmed that they were single, 1.2 nm steps, despite a quoted resolution of 1.5 nm under such conditions.

Fig. 4. Ibidem *high-resolution scanning electron microscopy* (*HRSEM*) and *atomic force microscopy* (AFM) measurements acquired on *zeolite A*: (a) split-screen *HRSEM*/AFM deflection image of the (100) surface, (b) AFM height image with a region chosen for an equivalent cross section, and (c) cross section showing 1.2 nm terraces.

1.3.4. Sample inclusions/impurities

The *BSE* contrast for inclusions that consist of heavy elements (such as gold) within a matrix of light elements (such as silicon) is larger than the *BSE* contrast for light-element inclusions (such as polystyrene on lead-free solder), to the extent that such inclusions are not usually visible (compare Fig. 5b with Fig. 5d). However, the *SE* contrast is high in both situations (compare Fig. 5a and c).

Inclusions of different materials are usually visible, provided that the size of the inclusions is at least as large as the beam diameter (and, therefore close to the resolution). Inclusions below the sample surface must be considerably bigger than the beam diameter; otherwise, they are not observed because of the spread of the electrons through the sample and the resulting beam broadening. The relation between beam diameter (spot size) and resolution is discussed below.

1.4. Factors that determine beam diameter

The theoretical calculation of the beam diameter is related to the empirically determined SEM resolution [26]. A certain minimum diameter of the electron probe (spot size) at the sample surface is necessary for high-spatial-resolution imaging. The diameter *d* of the impact electron beam is estimated as a disc of least confusion, *d*, as follows [23].

$$d = \sqrt{d_o^2 + d_d^2 + d_s^2 + d_c^2} \tag{6}$$

d_o, d_d, d_s and d_c are contributions to the disc from *the source size*, *diffraction*, *spherical aberration*, and *chromatic aberration*, respectively, which are expressed as follows:

$$d_0 = \frac{2}{\pi \alpha} \sqrt{\frac{I_P}{\beta}} \tag{7}$$

$$d_d = \frac{0.6 \cdot \lambda}{\alpha} \tag{8}$$

$$d_s = 0.5 \cdot C_s \alpha^3 \tag{9}$$

$$d_c = C_c \frac{\Delta E}{E} \alpha \tag{10}$$

I_P (A) = impacted electron-beam current, β (A m^{-2} sr^{-1}) = brightness of the electron source, α (rad) = impacted electron beam convergence angle at the sample position, λ (m) = wavelength of the impacted electron beam at the sample, Cs (m) = spherical aberration constant, Cc (m) = chromatic aberration constant, ΔE (J) = energy spread of the electron source, and E (J) = landing energy on the sample.

To reduce the spot size at low landing energy, we need to consider that brightness β is proportional to E, which requires the electron source with high β. If β is sufficiently high, d_0 term is negligible compared with d_d term in equation (6). We also need to consider that λ is inversely proportional to root E. Thus, convergence angle α should be increased, which cause d_s and d_c terms to increase. From equations (7)–(10), we understand that four factors affect the spot size at low landing energy: brightness β, energy spread ΔE, Cs, and Cc. An increase in brightness and reduction in energy spread is required to reduce the spot size, hence the move to field emission electron sources (see Table 1).

Beyond exploitation of field emission electron sources, improvement of objective lens, especially combination of magnetic field and electrostatic field is crucial for further reducing C_s and C_c.

Note: Equation (6) well describes the behavior of the beam diameter for our purposes. More accurate predictions require numerical wave optical calculations [27] or associated approximations using analytical models [28].

2. The importance of low voltage and signal filtering

Even with a minimal spot size and the large amount of signal from the sample, there are a great many factors that require the voltage of the impacted electrons to be as low as possible for the high-resolution surface imaging of nano-electric insulator materials.

2.1. Signal generation

SE detectors cannot distinguish between *SE1* and *SE2*: the latter is generated even at large distance away (approximately half the value of *R* given in Equation (1)) from the *impacted beam* as *BSEs*, which therefore reduces the resolution and topographic component in topographic-contrast images. Fig. 6 shows the trajectories of *interacting electrons* inside a sample and their decrease in range and exit area with decreasing the landing energy of *IEs*. The resolution
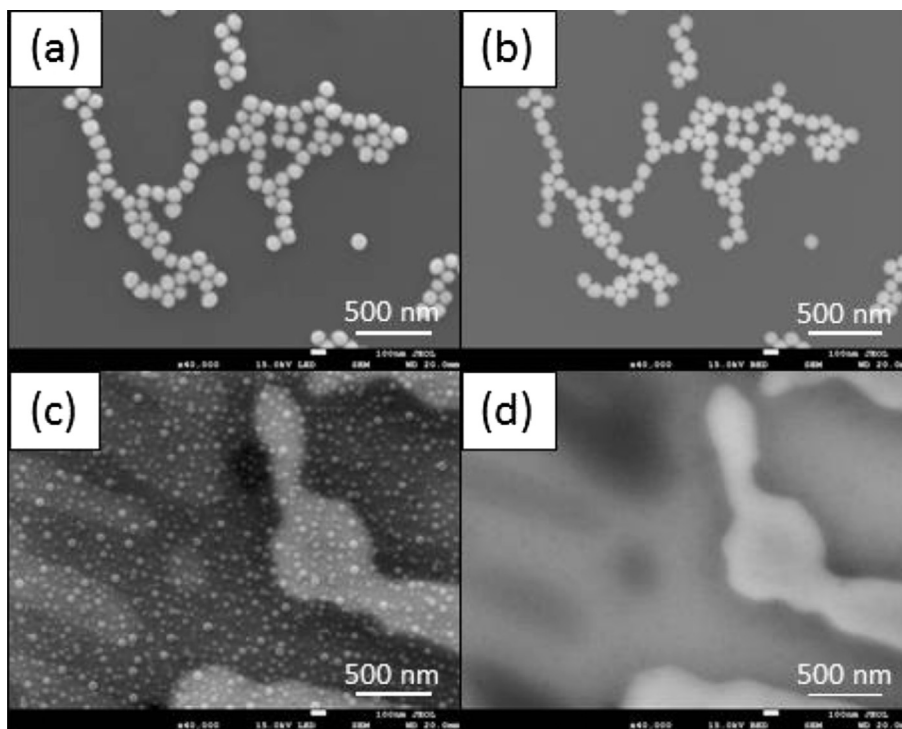
Fig. 5. Contrast between heavy and light elements in *SE* and *BSE* images. (a) *SE* image and (b) *BSE* image of gold (heavy element) on a silicon substrate (light element). (c) *SE* image and (d) *BSE* image of polystyrene particles (light element) on lead-free solder (heavy element). Conditions: Electron landing energy = 15 keV; Substrate bias = 0 kV; Working distance = 20 mm.

of *BSEs* is generally reported to be similar to their range [23,29]. A good approximation is given by Equation 1

At low landing energies, the spreading of *interacting electrons* is considered to be as small as the *escape depth of the SEs*. The resolution of the *BSE* image is therefore expected to be as good as that of the *SE1* image. The *SE2* component in the *SE* image will contain a great deal of spatial information, leading to high-contrast *SE* imaging. Therefore, information from the sample surface is easier to obtain using a lower landing energy in SEM, while information from the bulk is obtained when using a higher landing energy [30,31].

2.2. Charging effects

There are various *nano-materials* which are electrical insulators, such as *mesoporous silica*. To observe them using SEM, techniques to reduce charging up of specimens are required. Particular scan strategies to reduce charging; the reduction of the beam-irradiation time for each pixel or successive scan and the subsequent integration of the signal for each point is effective in reducing the charging effect. However, a reduced landing energy also reduces

Table 1
Properties of electron source most relevant to beam diameter [20]. Thermally excited electrons are ejected from a tip in a thermionic source. Thermally excited electrons are ejected beyond the barrier at source/vacuum interface while the barrier height is reduced by strong electric field in a Schottky field emitter. Electrons quantum mechanically tunnel from the source to vacuum in a Cold field emitter. Depending on the principle of the sources, brightness and energy spread differ significantly.

Electron source	Brightness (A/cm^2 sr)	Energy spread (eV)	Spot size (nm)
Thermionic	10^5–10^6	1–3	5000–100,000
Schottky field emission	10^8	0.3–1	15–30
Cold field emission	10^8	0.3	<5

the charging of the samples to some extent [37]. The *electron yield* (σ) is the ratio of the emitted electrons to *IEs* and is the sum of the *secondary electron yield* (δ) and the *backscattered electron yield* (η). An electron yield of less than 1 results in a negatively charged sample and thus a distorted image. σ increases with decreasing landing energy and often exceeds unity at low energy, while it begins to decrease again at extremely low energy (typically less than 500 eV). The conventional model predicts that charging does not occur when σ is unity, although the reality is more complex than the prediction of this simple model [37–40].

2.3. Beam damage

The reduction of the landing energy is an essential consideration in the reduction of the type of beam damage experienced by *nano-materials* in SEM. Unlike beam damage of biological TEM samples, for which the use of a cryo-TEM (a TEM in which the sample holder is cooled using liquid nitrogen or liquid helium) is encouraged to reduce the sample temperature and thereby stabilize the samples. The beam damage faced by crystallographers in SEM is of a non-biological (C-A) transition type [41], in which the *IEs* chemically alter the insulating sample. The beam damage is more severe in *mesoporous* and *MOF* crystals, which possess less-ordered chemical bonds and much weaker molecular bonding, respectively.

Fig. 7 illustrates the beam-damage phenomenon observed on crystal surfaces of *LTA*. Irreversible, sub-surface damage in the form of surface depressions of a maximum of 15 nm has been observed in *LTA*. The depth is proportional to the time of exposure, the magnitude of the current and the landing energy. The latter is proportional to the range of inelastic collisions and comparable to the size of the depressions (Equation (1)). This finding suggests that inelastic collisions are responsible for the chemical change and the subsequent collapse/densification/ejection of material.
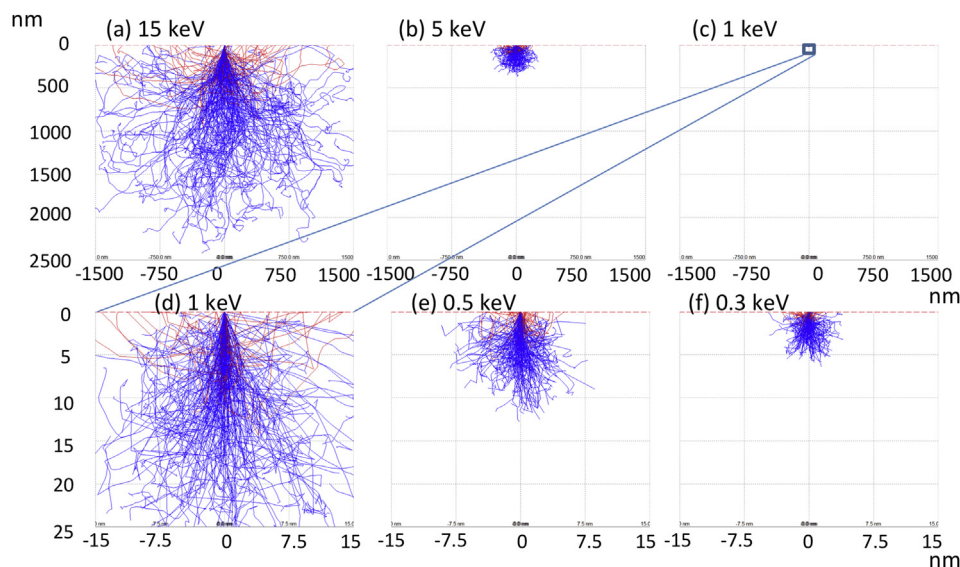
Fig. 6. CASINO Monte Carlo simulation [32,33] of the electron trajectories of electrons upon interaction with a bulk silicon sample. Electrons indicated in red are *BSEs*. In a typical Monte Carlo simulation, injected electrons are treated as particles. The direction change of a IE is described by elastic scattering (cross sections: see Equation (2)). The length of the straight path between elastic events is determined by the *mean free path*. The loss of energy of the electron is typically described by a continuous-slowing-down model [34−36]. (For interpretation of the references to color in this figure legend, the reader is referred to the web version of this article.)

The damage leaves the surface of the crystal structurally intact but with a reduced contrast. *Ibidem* AFM demonstrates that the terraces are resolvable with heights that differ by less than 5%. This suggests that the surface of the crystal is covered in a uniform layer of material, created during the damaging process, that masks the topographic contrast in the SEM image. The surface is not destroyed. The material is believed to at least partially originate from contamination because topographic-masking contrast may manifest even when there is no recorded damage to the rest of the crystal.

3. Low landing energy and signal-filtering methods

3.1. Combined objective lens

The objective lens, in addition to demagnifying the electron beam to a probe, can also help to filter the emitted electrons according to their utility, and decrease the energy of the primary beam rapidly before impacting with the sample.

3.1.1. History of combined lenses

Although the aberration coefficients for magnetic lenses are smaller than for electrostatic lenses at high beam energy, since high voltage is required for electrostatic lenses at high beam energy, while applicable voltage is limited due to discharge, the introduction of field-emission sources and the need for low-voltage SEM have directed attention toward electrostatic lenses [42,43]. The maximum electrostatic field is limited by the dielectric breakdown (discharge) for purely electrostatic lens, and the maximum magnetic field is limited by the saturation of the polepieces, which are pieces of magnetic material at a gap of magnetic lens, shaped to control the magnetic flux distribution. Both these drawbacks limit the shortening of the focal length and further reductions to spherical and chromatic aberrations.
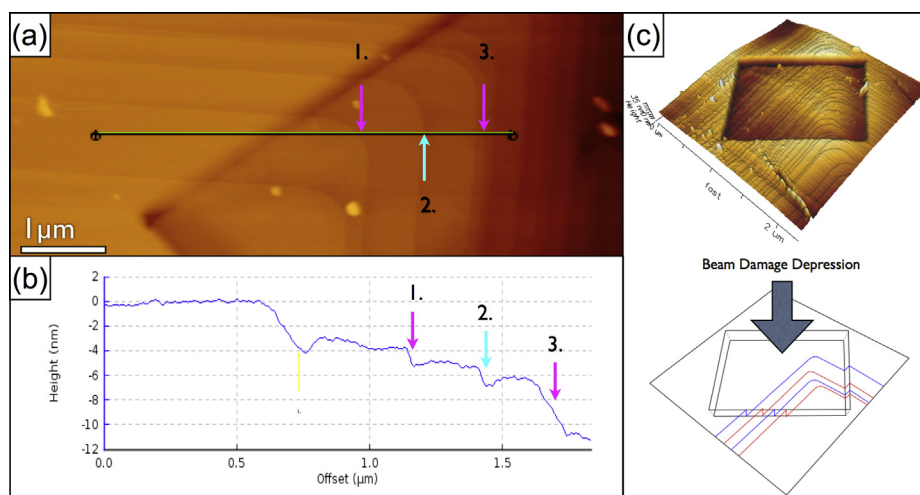
Fig. 7. AFM image and associated cross section (represented by the green line) of *zeolite A* (a) and (b). (c) Height trace and schematic of the conservation of surface steps despite depression formation. AFM images courtesy of Pablo Cubillas. (For interpretation of the references to color in this figure legend, the reader is referred to the web version of this article.)

Pease et al. (1967) experimentally demonstrated that a combination of a magnetic lens and a retarding electrostatic field permitted the further reduction of spherical and chromatic aberrations, and thus allowed the achievement of landing energies as low as 10 eV [44]. Yau et al. (1981) further investigated this type of lens combination to improve the spot size (although the primary purpose of this objective lens was low-voltage electron-beam lithography) [45]. They proposed two configurations:

a. A magnetic field is generated between the first and second polepieces, with a voltage applied between the second polepiece and the *target* (sample). In this case, the sample is immersed in an electrostatic field, but not in a magnetic field (Fig. 8a).
b. A magnetic field and an electrostatic field are applied between the first and second polepieces, and the target is placed onto the second polepiece. In this configuration, the sample is immersed in both an electrostatic field and a magnetic field (Fig. 8b).

The lens effect is achieved in both cases by applying a negative bias to the sample against the aperture thus immersing the aperture in a strong electric field. This produces a larger convergent force against the incident electrons to the sample, which shortens the focal length and generally results in smaller aberrations than those of independent systems [45].

Various other types of *combined lenses* (using both magnetic and electrostatic fields) have proposed and implement [43,46—51].

3.1.2. An application of specimen bias

The application of negative bias to the sample is one valuable method of generating an electrostatic field between the magnetic lens and the sample to act as a focusing and retarding field for the primary electrons, and an accelerating field for electrons emitted from the sample.

The SEM images of sputtered gold nano-particles on carbon obtained at a landing energy of 500 eV with different sample biases are shown in Fig. 9. The resolution of the SEM image is greatly improved with the bias from 0 to −5 kV.

3.2. Through-the-lens detection system

3.2.1. The working-distance problem

As described in 1.2, *ET detector* is still an important detector for current commercially available equipments. *ET detectors* placed outside of the optic column are referred to as *lower ET-detectors* (*LEDs*) to avoid confusion with *ET detectors* that combine a scintillator and photomultiplier. *LEDs* detect *SE1*, *SE2* and *SE3* (see Fig. 3) [20,22].

A short *working distance* (*WD*, the distance between the objective lens and the sample) decreases the detected amount of *SE1* and *SE2* relative to *SE3*. The sum of *SE2* and *SE3* may reach 89% of the total signal for high Z sample of gold [20], thereby reducing the high-resolution topographic component of the image.

The pattern of images shown in Fig. 10, taken at short *vs.* long working distances (see Fig. 10d and f compared to Fig. 10a and e, respectively), closely resembles to the examples given in Fig. 5 for *BSE* images *vs. SE* images (note the inability to differentiate the light polystyrene inclusions from the heavy solder substrate at short *WDs*). This observation, in combination with the fact that *SE2* and *SE3* are generated from *BSEs*, and not *SEs*, demonstrates that the *LED* is *effectively* (though not literally) a *BSE* detector at a short working distance, as has been reported elsewhere [52].

On the other hand, the detection of mainly *SE1* and *SE2* using *LEDs* requires a long *WD*. However, a long *WD* has a negative impact on the spot size, and ultimately, the resolution. An alternative possibility is to place the detector within the lens itself: such a configuration is called a *through-the-lens* (*TTL*) detection system.

3.2.2. TTL detectors

WDs of less than 3 mm are possible with *TTL detectors*, which allows the acquisition of high-resolution observations. Current high-resolution commercial *FE-SEMs* frequently adopt *TTL detection systems* [16].

The application of a negative substrate bias, in addition to reducing the landing energy, improves the detection efficiency because the *BSEs*, particularly *BSEs* with relatively lower energies, are accelerated toward and through the column. *SEs* are simultaneously accelerated into the column and may be detected using a *different TTL detector* with the application of *energy filtering*.

3.2.3. TTL with filtering

A typical *TTL-with-filtering* system (referred to by JEOL as the *JEOL System*) is introduced here, using the JSM-7800F (and JSM-7100F TTL − JEOL Ltd.) as an example (Fig. 11). *TTL-with-filtering* systems have a *LED* outside of the column; and two *TTL detectors* inside a SEM column (*the upper electron detector* (*UED*) and the *upper secondary electron detector* (*USD*). The biased grid between the *UED* and *USD* acts as a *high-pass filter* so that primarily *BSEs* of high energy are selectively detected using the *UED*, and *SEs* of low energy are reflected by the grid and collected by the *USD*. The application of a positive bias to the grid allows the *UED* to become a mixed-signal detector that collects both *SEs* and *BSEs*. The
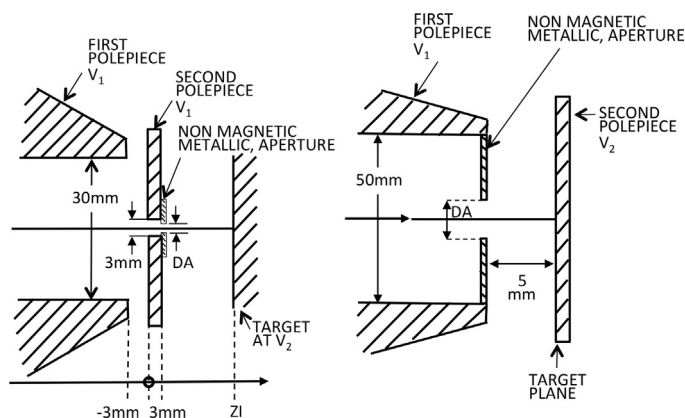
Fig. 8. Schematic of objective lenses implemented by Yau et al. [45]. (a) a magnetic field is applied between the two polepieces, so the sample is not immersed in a strong magnetic field. (b) the sample is placed on a magnetic polepiece, so the sample is immersed in the magnetic field.
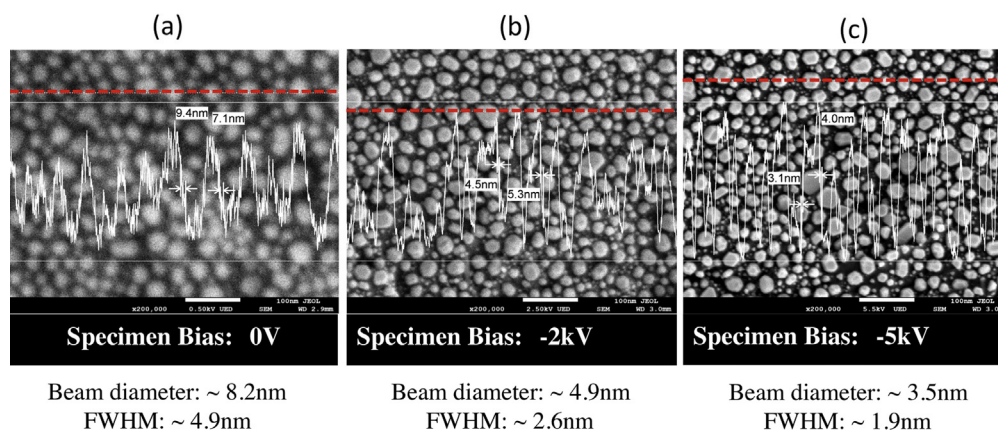
Fig. 9. SEM images with increasing substrate bias from (a) 0 V to (c) −5 kV. The red line indicates the position for the line profile. Assuming a Gaussian distribution, the resolution improves. Conditions: JSM-7800F with *GBSH* (*Gentle Beam Super High resolution*), which allows a specimen bias of down to −5 kV; Landing energy = 500 eV. (For interpretation of the references to color in this figure legend, the reader is referred to the web version of this article.)

application of a substrate bias increases the upward velocity of the *BSEs* allowing more efficient collection (Fig. 11b).

TTL-with-filtering systems have been used as *LSI* (Large-Scale Integrated circuit) *testers* to detect electric potential of *LSIs* [53,54,46].

4. Images collected using a combined lens and a TTL detection system with filtering

4.1. Mesoporous LTA

A *HRSEM* investigation of the *mesoporous LTA* after *cross-section polishing* (CP) revealed the presence of a disordered network of *mesoporous channels* that penetrated the *microporous zeolite crystal*

[55]. This *mesoporous LTA* has been synthesized by Ryong Ryoo's group under hydrothermal synthesis conditions that incorporated a quaternary ammonium-type organosilane surfactant. *Mesoporous LTA* is highly electron-beam irradiation sensitive. Possibility of beam damage reduction by lowering landing energy reduction is investigated.

The image obtained using a landing energy of 80 eV exhibits lesser edge effect because of small interaction volume [30]. Landing energies of 1 keV and above produced beam damage (Fig. 12).

4.2. IRMOF

MOFs are made by linking inorganic and organic units. They have large pores inside their crystals and are effective at gas
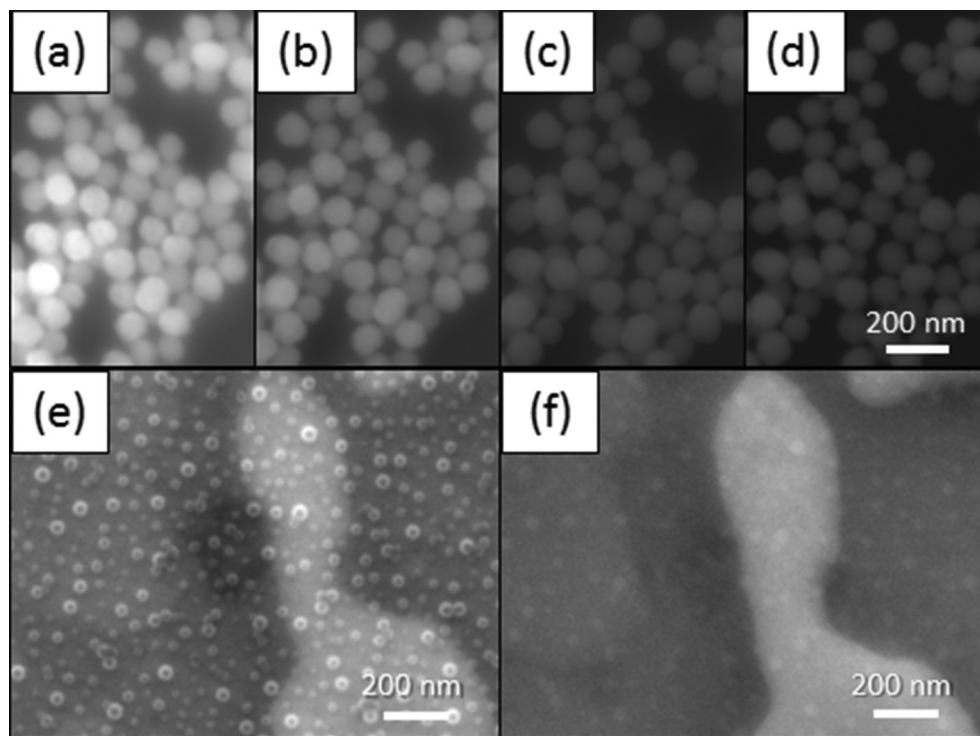
Fig. 10. Working-distance dependence of contrast for images acquired using the *LED*. (a–d) Gold nano-particles on silicon substrate. Left to right: *WD* = 20, 10, 5, and 3 mm. The contrast and brightness were kept constant. (e) Polystyrene particles on lead free solder substrate. *WD* = 20 mm. Predominantly an *SE* image. (f) Polystyrene particles on lead free solder. *WD* = 5 mm. Predominantly a *BSE-like* image. JEOL JSM-7800F.
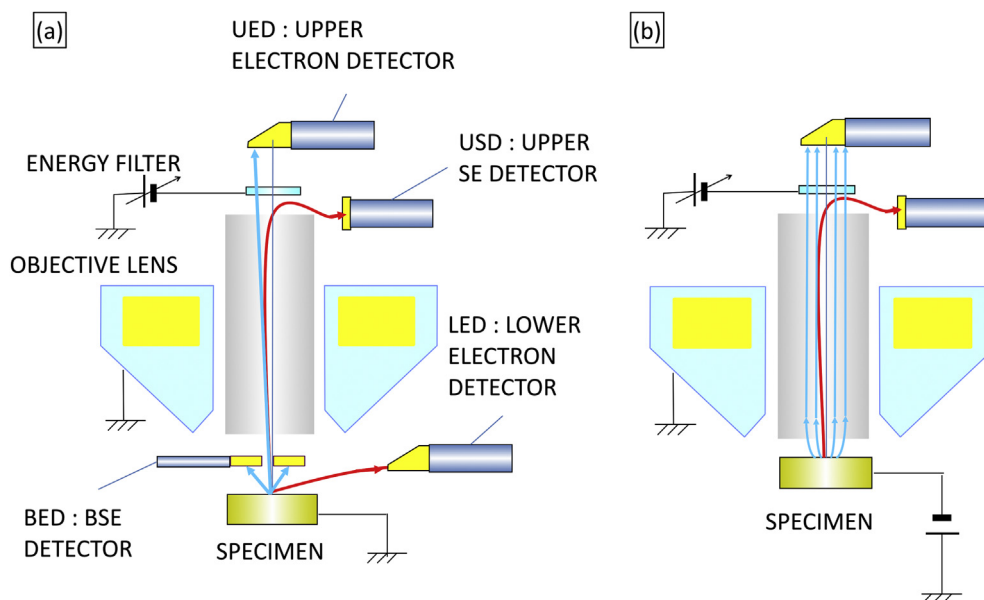
Fig. 11. Schematic diagram and the typical trajectories of *SEs* and *BSEs* for JSM-7100F TTL and 7800F: (a) without substrate bias and (b) with substrate bias. *SEs* and *BSEs* are selectively detected using electrodes, *the energy filter,* and *four different detectors*.

storage, separations and catalysis. Since linker length is controlled exactly, *pore size is precisely controlled*. To investigate the connections of pores to the surface is very important, since the connections are critical for the performances of the storage etc. Therefore, not only the pore structure is investigated using TEM, but also the surface structure of the *MOFs* was investigated using *HRSEM*.

An isoreticular series of MOF-74 structures (termed *IRMOF*-74-I to XI) with pore apertures ranging from 1.4 to 9.8 nm has been synthesized by Omar Yaghi's group [56].

Fig. 13b shows a C_s-corrected *High-Resolution TEM* (*HRTEM*) image. The electron-beam damage to the specimen was minimized as much as possible by minimizing the beam density and compensating for the associated reduction in the *signal-to-noise ratio* (S/N) through the superimposition of individual frames. (The *HRTEM* image is an accumulation of 7 frames, each with a 0.5 s exposure time, after drift compensation. Fig. 13c was acquired via SEM at an electron landing energy of 300 eV after application of the *Gentle Beam Super High resolution* (*GBSH*) technique for the JSM-7800F. Hexagonally arranged pores of ∼3.5 nm in diameter can be clearly observed. The connectivity of the pores to the surface is clearly shown by a SEM observation.

4.3. Helical TiO₂

Chiral TiO₂ nanofibers with electron-transition-based optical activity have been synthesized by Shunai Che's group via the

transcription of the helical structure of amino-acid-derived amphiphile lipid enantiomers through coordination-bonding interactions [57].

The chiral fibers were ∼25 nm in width with a ∼100 nm pitch length along the fiber axis. The small size of the features, made observation of the fine details of the helical morphologies by SEM very difficult. The morphology of the fibers was realized by *HRSEM* by application of a (high resolution) high column energy and low landing energy through the application of specimen bias (Fig. 14a and Fig. 14b). The corresponding *HRTEM* image and model are presented in Fig. 14c and d, respectively, showing inner tubular structures of ∼12 nm in diameter along their central axes. The as-prepared amorphous hybrids were converted into crystalline TiO₂ with stacks of anatase nanocrystals of ∼20 nm in size via calcination (Fig. 14e–g).

Since the calcined sample was more stable against the beam, higher landing energies were used to achieve a higher resolution. The associated increase in charging was reduced through the use of a shorter working distance. Fig. 14f shows an *HRTEM* image of an array of nanocrystals that exhibit contrast close to the <111> zone axis of the anatase structure. The adjacent nanocrystals have a rotational misplaced arrangement, piling up by sharing one of their {101} facets while keeping one <111> axis in common, leading to a helical array of nanocrystals with nearly parallel <111> axes (Fig. 14g). It is very difficult to determine the structural relations of all the nanocrystals from these results only, because of the
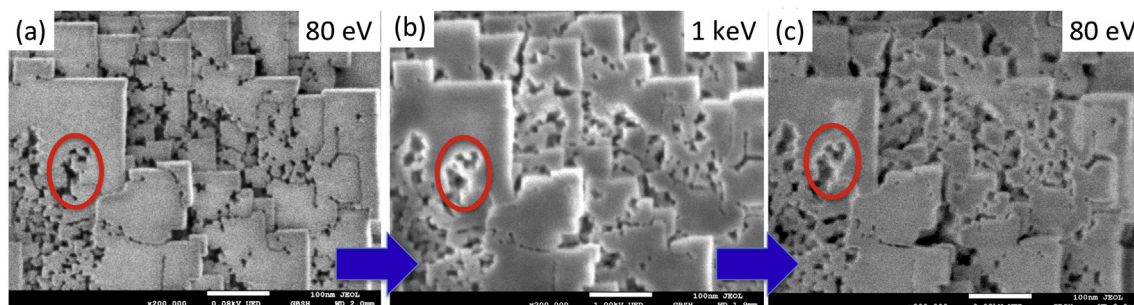
Fig. 12. SEM images of *mesoporous LTA* acquired at low landing energy, thereby reducing the effect of beam damage. Conditions: Specimen bias = −5 kV.
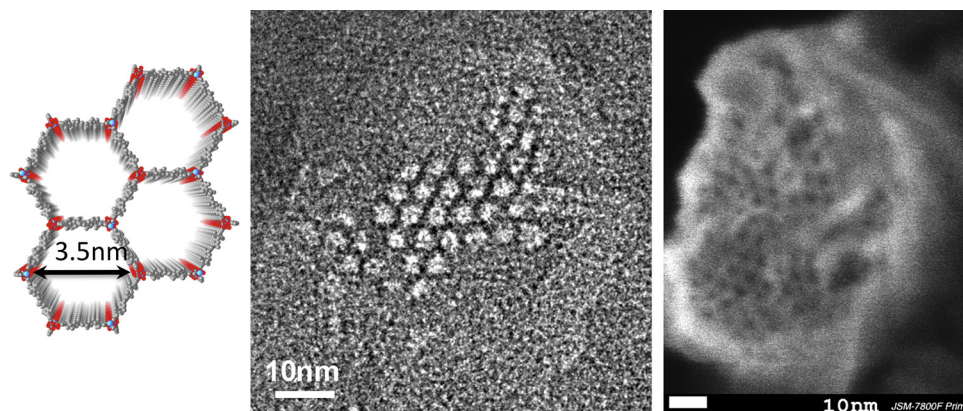
Fig. 13. (Left) Schematic drawing, (center) TEM image, and (right) SEM image of *IRMOF*-74-VII. Pores of 3.5 nm in diameter can be clearly observed. TEM conditions: JEM-2010F FEG-TEM; Accelerating voltage = 120 kV; CEOS post-specimen spherical aberration corrector; Beam density = 50–130 electrons/nm^2. SEM conditions: Beam current = 2.0 pA. Landing energy = 300 eV. Sample bias = −5 kV through *GBSH*.

overlapping crystals and the small crystal size. Based on the initially formed double-helical structures, we suggest that the crystallization process occurred locally while retaining characteristics of the double-helical morphology of the as-prepared samples, despite the disappearance of the hollow tubular structures.

Both the amorphous and the post-calcined anatase crystalline helical TiO$_2$ fibers exhibited an optical response to circularly polarized light at the absorption edge near ~350 nm. This response was attributed to the semiconductor TiO$_2$-based electronic transitions from the valence band to the conduction band under an asymmetric electric field [57].

4.4. Mesoporus silica crystal (SBA-15)

Mesoporous silica crystal, *SBA-15*, has 2D-hexagonally arranged primary mesopores (*channels*) of the plane group *p*6*mm*. The crystal has a highly complex porosity with unordered pores that penetrate the amorphous silica wall in addition to the main mesopores [58]. Changes to the formation sequence lead to varying degrees of *plugs* within the mesopores, potentially sealing the mesopore's off from the exterior, making the mesopores inaccessible to chemical reagents or probing gas molecules. Owing to these porosities, *mesoporous silica* is expected as gas storage and catalysis. The
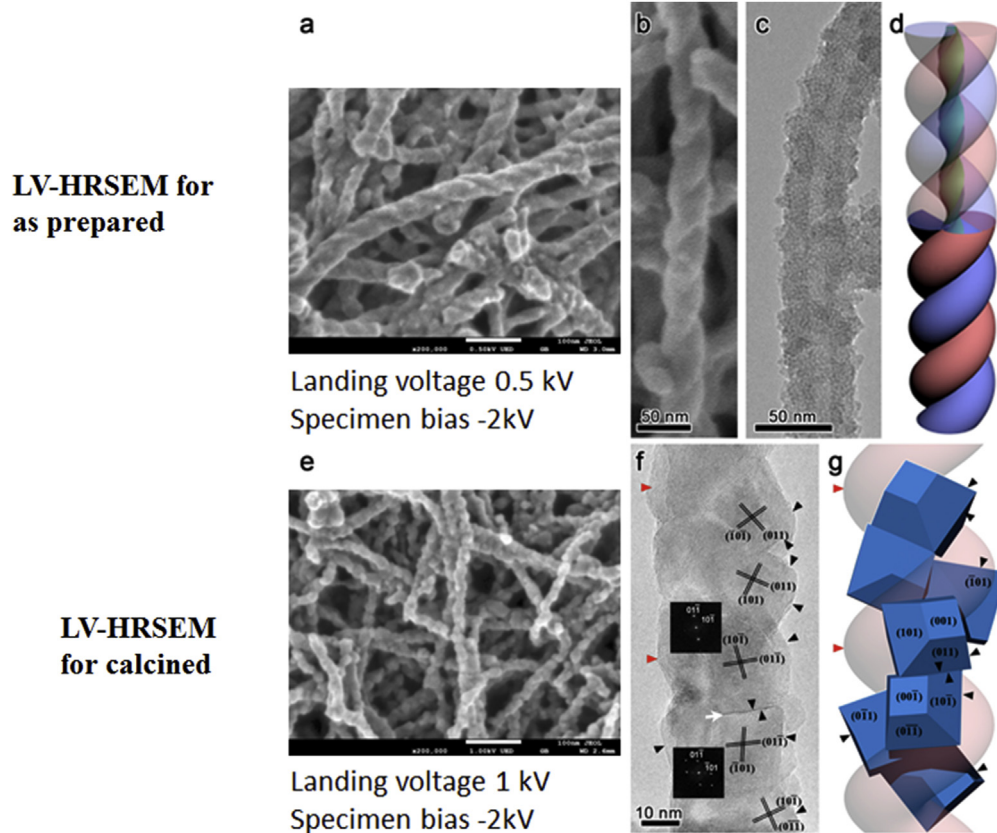
Fig. 14. Helical TiO$_2$ of an as-prepared organic lipid: (a & b) *HRSEM* images. Conditions: Landing energy = 500 eV; Sample bias = −2 kV; *WD* = 3 mm. (c) *HRTEM* image. Accelerating voltage = 200 kV; (d) Schematic drawing. Calcined chiral crystalline hybrid TiO$_2$ fibers: (e) HRSEM image. Conditions: Landing energy = 1.0 keV; Specimen bias = −2.0 kV; *WD* = 2.2 mm (f) *HRTEM* image. Accelerating voltage = 200 kV; (g) Schematic drawing.

connections of these pores to the surface are again important for the performance. Although nitrogen sorption generally provides valuable information regarding the porous character of *mesoporous materials*, only direct observation can unveil detailed information concerning the porosity.

HRSEM of *SBA-15* suffers particularly strongly from *charging effects*. A specimen bias was therefore applied to lower the landing energy to 300 eV and increase the electron yield. Maintaining a constant landing energy and beam current demonstrated that an increase in column energy and specimen bias (*cf.* Fig. 15b with Fig. 15a) improved both the resolution and S/N. Both inter-channel micropores and plugs within channels can be observed in Fig. 15c.

4.5. Au@TiO₂ yolk-shell material

Gold yolk-shell materials, Au@TiO₂, Au@ZrO₂ and Au@C, have been synthesized via nanocasting of gold nano-particles within porous-walled, hollow spherical shells (or *supports*) of TiO_2, ZrO_2 and carbon. Synthesis via the *silica route* can produce Au@SiO₂@X (where $X = TiO_2$, ZrO_2 and carbon), where the SiO_2 core is then selectively removed using aqueous NaOH. The catalytic potential of the pore-walled supports, the intrinsic catalytic activity of gold nano-particles and the highly structurally and compositionally defined yolk-shell particles, even at high temperatures, make these types of material ideally suited for discriminating the effects of support and particle size for mechanistic studies of heterogeneous catalysis [59].

The *electron diffraction* (ED) pattern and the *HRTEM bright-field* (BF) image (Fig. 16a and b, respectively) reveal that TiO₂ possesses an anatase structure with a regular truncated tetragonal bipyramidal morphology. The gold particles are spherical, with a diameter of approximately 17 nm, and sometimes twinned (not shown here).

TTL with filtration, biased at −500 V, allows the *USD* and the *UED* to *simultaneously* collect electrons of low and high energy, which predominantly correspond to topological *SEs* and compositional *BSEs*, respectively (Fig. 16d and e). The resolution of the *BSE* image obtained using *UED* can be improved by increasing the specimen bias, as expected: this improvement is illustrated by the differences among Fig. 16f–h. (The landing energy and beam current were kept constant.)

5. Other applications of backscattered electrons

5.1. The potential of highly resolvable BSE1

The potential resolution of *BSEs* is not well clarified [29]. However, it has been experimentally reported that high resolution can be obtained in *BSE* images [60,61], possibly through the detection of *BSE1* instead of *BSE2* (*BSE1* and *BSE2* are originally called *BS1* and *BS2* by Joy in his paper) [29]. The former is scattered near the incident point of the *IEs*, resulting in high-resolution contrast, while the latter is generated deep within the sample (the size and shape of this signal is simulated in Fig. 6), thus result in less-resolvable image definition, as intensive investigation by Merli et al. [62] have shown. An example is given in the contrast of Fig. 5b and d, where the former has a strong *BSE1* signal component, while the latter's *BSE1* signal cannot be identified because of the high *BSE2* background that arises from the presence of a low *BSE* coefficient of the material. Angle selection may allow the collection of information regarding topology, crystalline direction, and/or composition [63].

5.2. Low loss electrons

It is possible to filter *BSEs* based on energy as well as angle. Wells et al. have proposed to improve the resolution of *BSE* images by detecting energy-selected *BSEs* [64]. Joy has also noted that *BSE1* (described in Section 5.1) corresponds to LLE (following
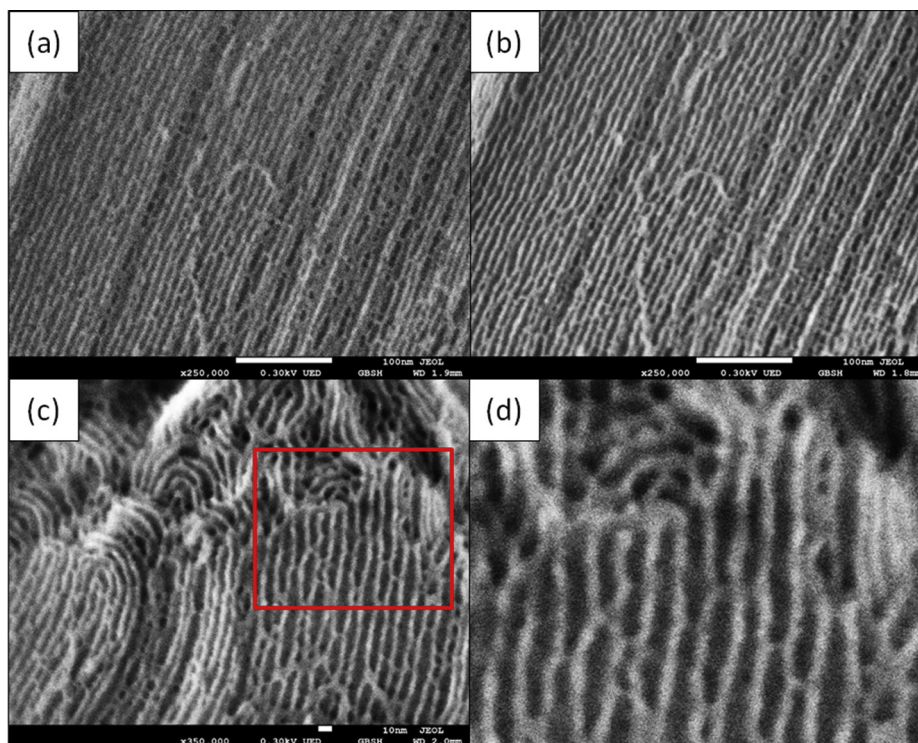
Fig. 15. *HRSEM* images of *SBA-15*. Conditions: landing energy = 300 eV; Beam current = 5.5 pA: (a) Specimen bias = −2 kV; (b) Specimen bias = −5 kV. (c) Landing energy = 300 eV; Specimen bias = −5 kV; Sample Ar ion cleaned for 10 min at 300 eV. Micropores can be clearly observed. (d) Digital magnification of (c).
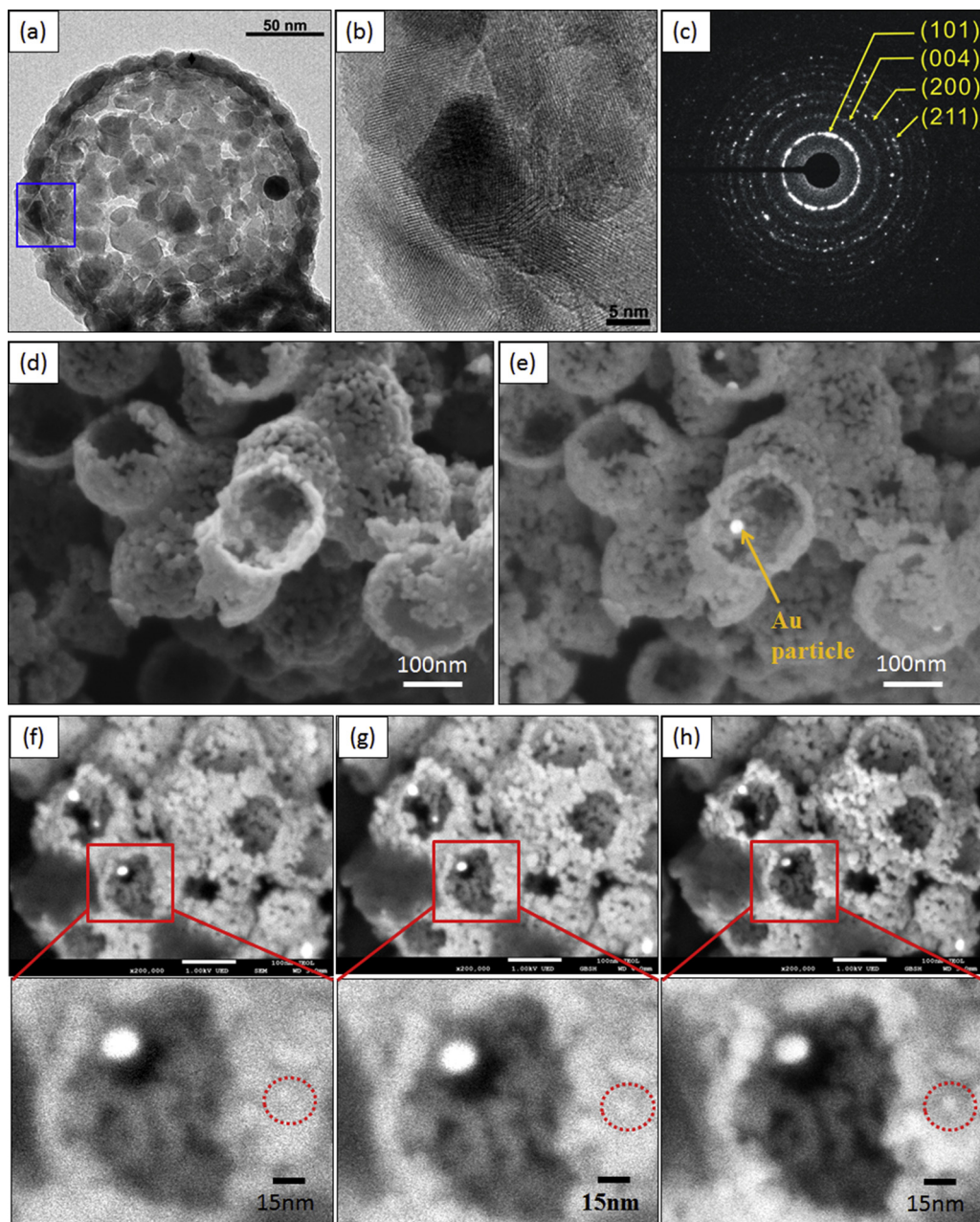
Fig. 16. Nanostructural analysis of Au@TiO₂ using (a−c) TEM (ARM-200F) and electron-energy-filtered SEM images providing mainly (d) *SE* and (e) *BSE* information, (f–h) demonstrate the resolution improvement in the *BSE* image that can be achieved by applying sample bias. Conditions: Electron landing energy = 2 keV; UED energy filter bias set to − 500 V, 1 kV; and beam current = 50 pA, respectively.

explanation) and selective BSE1 improves spatial resolution [29]. The basic principle is described below.

Fig. 17 shows the Monte Carlo simulation results obtained with different cut-off energies of electrons inside a sample for a landing energy of 500 eV. Here, the cut off energy is the energy at which the calculation is terminated for each trajectory. The maximum energy loss of an electron is the energy of the *IE* minus the cut-off energy. *BSEs* with small energy losses are called *low-loss electrons* (*LLE*) [64], although no quantitative definition exists. As the cut-off energy increases, corresponding to a decrease in the energy loss, the spreading of the interacting electrons inside a sample decreases. Thus, it is expected that the resolution can be improved using *LLEs*. This is the basis of the proposal developed by Wells.

The BSE signal contains information from both shallow and deep regions. From the Monte Carlo calculation results presented in Fig. 17, we can select the signal-generation depth by selecting the energy of the *BSEs*: using *LLEs*, we can obtain information from the shallow region. This energy selection has a similar effect to decreasing the landing energy of the *IEs*. If a structure is present near the surface, the contrast produced by it becomes strong when *LLEs* are detected, because signals from deeper regions are omitted. In other words, we can eliminate the background signal originating from deep inside the sample. If a structure is present at deep position, it cannot be observed using *LLEs*. If the sample has a uniform structure from the surface to deeper position, the resolution improves, as demonstrated by Merli et al. both theoretically and experimentally [65]. Meanwhile, the signal amount decreases with
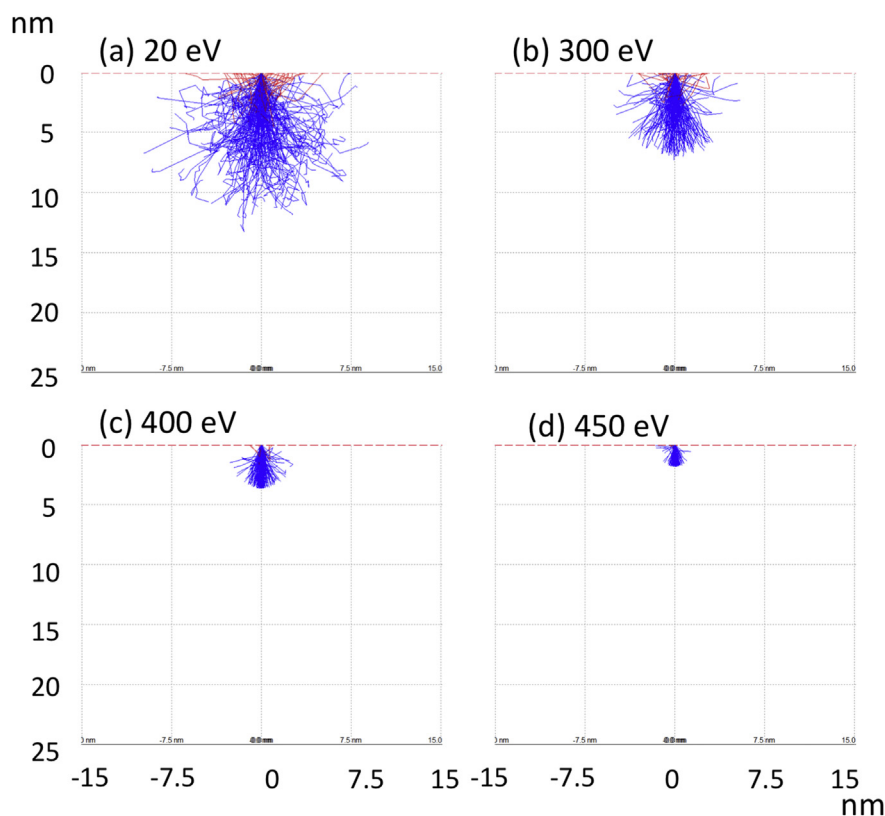
Fig. 17. Monte Carlo simulations of *low-loss electrons* (*LLE*) depicting the *IE* spreading in a sample for various *IE* cut-off energies. As the cut-off energy increases, there is a corresponding decrease in the energy loss and spreading of the electrons within the sample. Landing energy = 500 eV.

increasing the cut-off energy. Thus, the *signal-to-noise ratio* (*SN*) may degrade. An optimized choice of the energy cut-off should exist. Merli et al. have calculated the optimal energy loss for the cross-section of a semiconductor superlattice- sample by balancing the competing effects of contrast enhancement and *SN* degradation [65].

The *LLE* method is especially suitable for *high-BSE* samples. In comparison with lowering the landing energy to obtain surface information, *LLE* also offers the advantage of a smaller beam diameter, as a higher landing energy of the *IEs* can be used, offering higher resolution. Further experimental investigation of this approach is needed.

5.3. Atmospheric SEM

In conventional electron microscopes, samples are placed under vacuum. Thus, it is not easy to observe dynamic phenomena in liquid or gas. In addition, wet samples such as biological samples require time consuming sample preparation including dehydration and dryness. To overcome these problems, atmospheric scanning electron microscope (ASEM) has been developed. In the detection of *BSEs* from structures near the surface of a sample, samples placed under liquids or atmospheric gases can be imaged at high resolution [66—68].

5.3.1. Concept and structure of atmospheric SEM

Soon after the invention of electron microscopes, there was a demand for a chambers that could operate at atmospheric pressure. Abrams and McBain attempted to observe gaseous and aqueous samples in a TEM by placing such samples between two *electron-transparent collodion films* in a capsule [69]; this type of capsule, after further development and improvements, later became known

as *environmental cell* (*EC*) [70—72]. The production of tougher and thinner film via micro-fabrication using *Micro-Electro-Mechanical Systems* (*MEMS*) technology has further improved the *EC* applications [73—76].

A schematic diagram of a common ASEM setup is shown in Fig. 18. The ASEM dish (Fig. 19a—b) is placed above the inverted SEM column. A 100-nm-thick Si_3N_4 film (the exact composition of which can vary due to the chemical-vapor-deposition method of fabrication and is therefore more generally referred to as *SiN*) window at the bottom of the ASEM dish separates the vacuum from the sample, which is at atmospheric pressure. The Si_3N_4 film is thin enough to minimize any significant *IE* spread, thus permitting the high-resolution observation of samples under atmospheric pressure [66—68].

5.3.2. Colloidal silica − observation of dynamic phenomena in liquid

To investigate the capability to observe samples in liquid, colloidal silica particles in liquid (bright spots of 1 μm in diameter − Fig. 20a—c) have been continuously observed using ASEM. The trajectories of two particles, which are shown in Fig. 20d, demonstrate that their random motion is caused by the movement of the surrounding water molecules. The strong electron beam gathered positively charged silica particles into a closed packed structure (Fig. 20e—h). A reduction in magnification from ×10,000 to ×5000 (and therefore a reduction in current density) resulted in a gradually dispersal (Fig. 20i—l) [77].

5.3.3. Gold deposition − observation of electrochemical phenomena

The electrochemical deposition of gold can be observed in an ASEM system fitted with an electrochemical cell, as depicted in Fig. 19c—d. The two electrodes consisted of a 30-nm-thick Ti layer
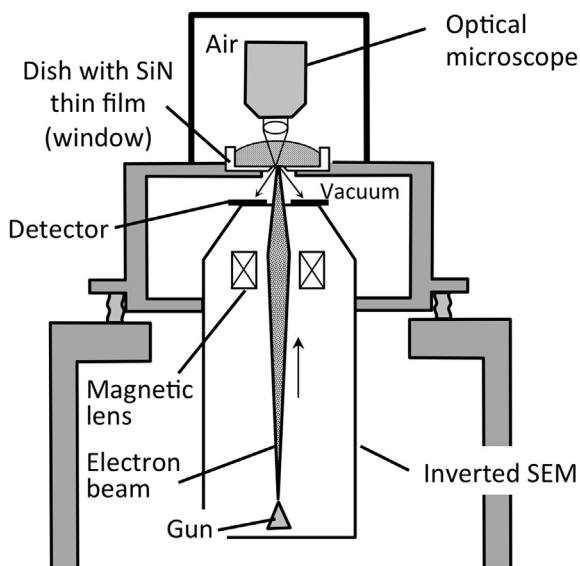
Fig. 18. Schematic cross-sectional view of Atmospheric SEM (ASEM specifically, the *ClairScope*™ system JASM-6200, JEOL Ltd.). An Si_3N_4 film separates the vacuum from the sample, which is under atmospheric pressure. An inverted scanning electron microscope located under the dish focuses an electron beam onto the sample through the Si_3N_4 film. The detector, which is located in vacuum, captures the electrons backscattered from the sample after they are transmitted back through the film. The optical microscope (OM) above the dish observes the same sample area as the ASEM.

and a 100-nm-thick Au layer on the Si_3N_4 film, which was patterned using conventional photo-resist and wet etching methods [78,79]. A dynamic phenomenon occurred near the cathode within 2.4 s of the application of current in the form of tree-like contrast (Fig. 21). The tree-like deposition was confirmed to be gold in a later SEM-EDS (Scanning Electron Microscope – Energy Dispersive X-ray Spectrometer) analysis and was speculated to have formed via the electrochemical migration processes with chloride ions [80].

The measurement of deposition formation at both mesoscopic and microscopic resolutions in real time using ASEM can aid in understanding the factors that influence deposition shape.

5.3.4. COS7 – observation of biological cells

COS7 cells may be imaged using both an optical microscope (OM) or ASEM. Such imaging requires culturing in an ASEM dish and the sequential staining of the endoplasmic reticula with both a fluorescent dye and a heavy-metal dye to allow the *ibidem* observation of contrast in the corresponding microscopes (*cf* Fig. 22a–b and c–e). The contrast of the ASEM images is also enhanced using charged-nanogold particles [81].

ASEM is therefore able to observe the microstructure of cells in solution at higher resolution than OM (An ASEM resolution of 8 nm has been recorded elsewhere using a sample of WGA-gold (15 nm) as a label [68]). Because of a very short sample-preparation time (less than 20 min), cells can be fixed and stained at decisive moments in biological processes, making ASEM very suitable for research regarding drug administration, among other applications [82–84].

5.4. Electron channeling contrast imaging (ECCI)

ECCI has been proposed to observe dislocations using SEM. Its potential advantages over TEM, for which it is necessary to make thin sample in order to transmit electrons, include the following: reduction in sample destruction, and in preparation time and resources; the capability of *in-situ* analysis, as bulk sample is observable within the depth of *BSE* generation (approximately half of *R* in equation (1)); the reduction in artifact formation; a more holistic view permitting comparison of dislocations on more macroscopic scale including the effects of grain boundaries, intrusions, extrusions and cracks [85], the crystallography of grains, and other heterogeneities of microstructure that are required, for example, in high-strength steel, and the observation of low-dislocation-density samples [85].

The basic concepts and history of *ECCI* have been well described in review papers [86–88]. When the electron beam is injected to
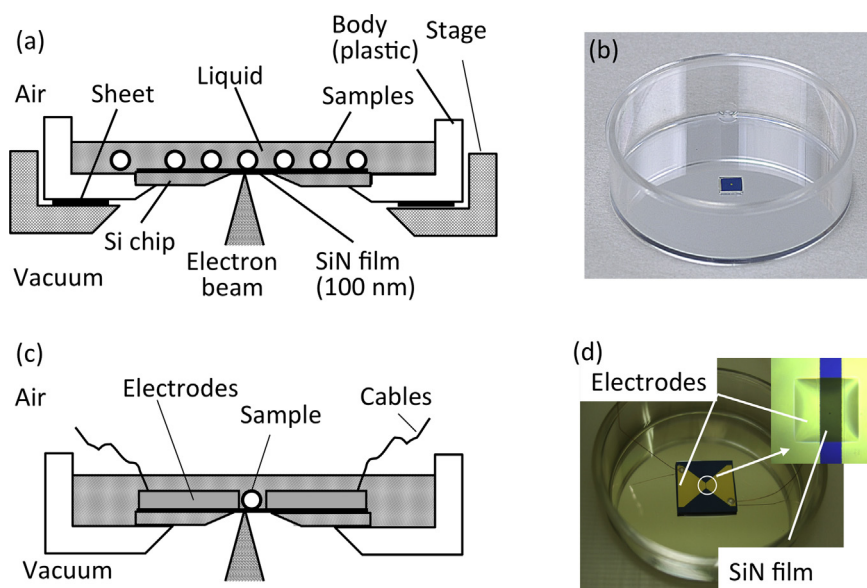
Fig. 19. Structure and characteristics of ASEM dishes. (a) Schematic cross-sectional view and (b) photo of a standard ASEM dish. A Si chip with an Si_3N_4 film window is placed in a polystyrene body, which is placed on the ASEM. (c) Schematic cross-sectional view and (d) photo of an electrochemical ASEM dish. The basic structure is similar to that of the standard dish, however, electrodes at 100 µm apart are fabricated on the Si_3N_4 film of the dish. Cables attached to the electrodes apply current between them.
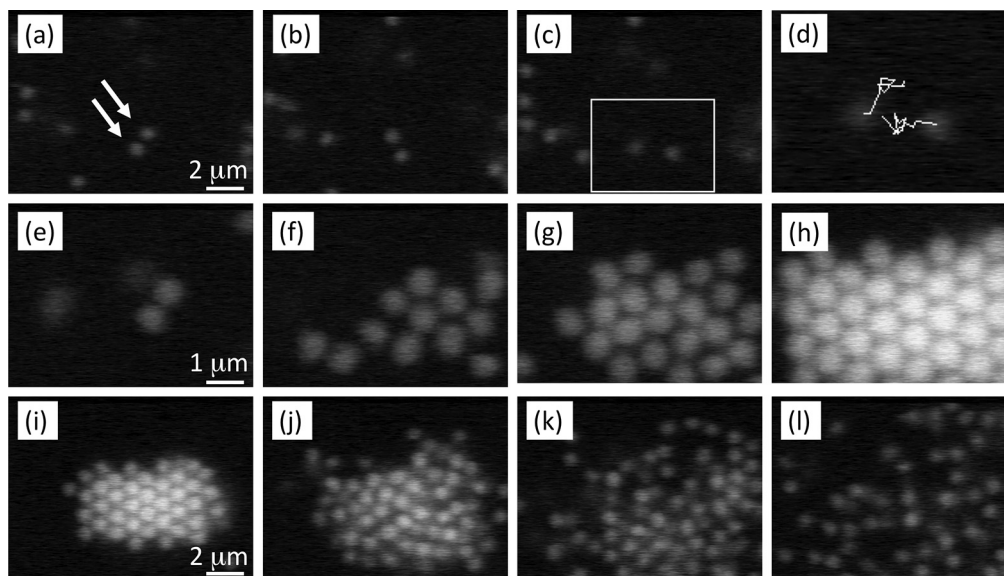
Fig. 20. *In situ* ASEM images of colloidal silica particles in liquid. (a–c) $M = \times 5000$. Time between each image = 0.5 s. The 1-s trajectories of the two particles indicated by arrows in (a) are superimposed on an enlarged image of (c) in (d). Random motion of the particles was observed. (e–h) $M = \times 10{,}000$; these images demonstrate radiation-induced self-organization. The time between (e) and (f) was 1 s, the time between (f) and (g) was 4 s, and the time between (g) and (h) was 20 s (i–l) Dispersal. The time between each image was 2 s.

one point and the angle incidence into the sample is varied (so-called *beam rocking*), the dependency of the *BSE* strength on the angle can be obtained. This is called the *electron channeling pattern* (*ECP*) [89]. Scanning *IEs* across a crystalline sample with an appropriate incidence angle produces BSEs whose intensity dependent on the lattice plane of the sample, thus producing *ECCI*. Crystal defects are observable using *ECCI* because they usually are accompanied by a change in lattice planes [86–88].

A typical *ECCI* image is shown in Fig. 23 for a fatigued copper crystal [90,91]. A ladder-like dislocation structure of persistent slip bands is visible.

It is necessary to know the direction of the lattice plane prior the *ECCI* observation. *ECP* has been widely applied for this purpose, though its spatial resolution is usually limited. In contrast, *electron*

backscattering diffraction (*EBSD*) is often used to determine the direction of the lattice plane for *ECCI* [85,92]. The spatial resolution of *EBSD* is approximately 30–50 nm, so *the combination of EBSD and ECCI* can improve the spatial resolution. The recent improvement in the analysis for *EBSD* allows lattice plane directions to be determined more easily. *ECCI* can permit the visualization of microstructural features that are not well captured by *EBSD*, such as single dislocations, dislocation substructures (*e.g.* cells), twins, grain boundaries and deformation bands [93].

Recently, *ECCI* has been applied to the analysis of practical steels [85,94–96] and semiconductors, including SiC, GaN, and SiGe [87,97,98]. Because *ECCI* can image features of dislocations at the nanometer scale, it will be valuable for future observation of *nanomaterials*.
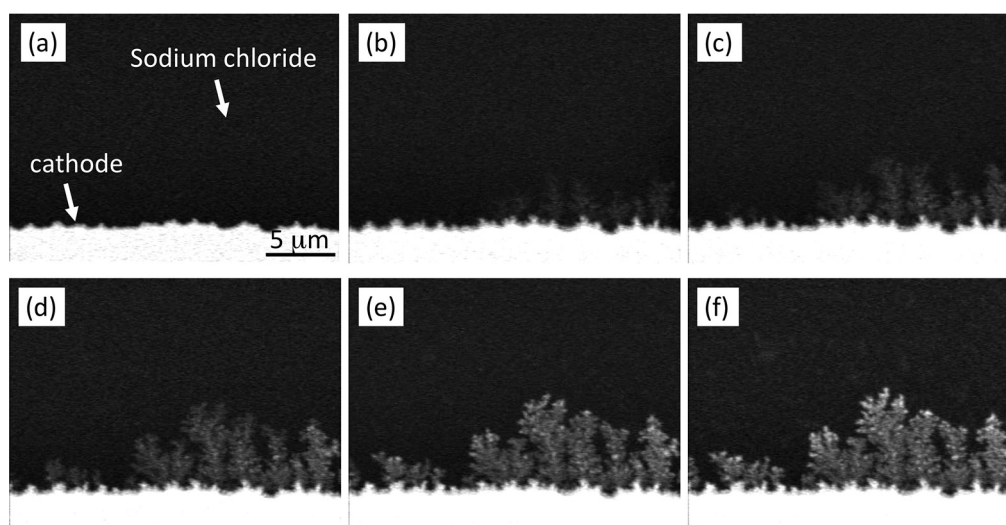
Fig. 21. *In situ* ASEM images of electrochemical deposition, under current flow between two electrodes in sodium chloride solution. (a) Region near the gold cathode, immediately after the application of voltage. The interval between (a) and (b) was 2.4 s, that between (b) and (c) was 0.6 s, that between (c) and (d) was 1.0 s, that between (d) and (e) was 2.0 s, and that between (e) and (f) was 2.0 s. A tree-like structure appeared (b) and grew (c–f).
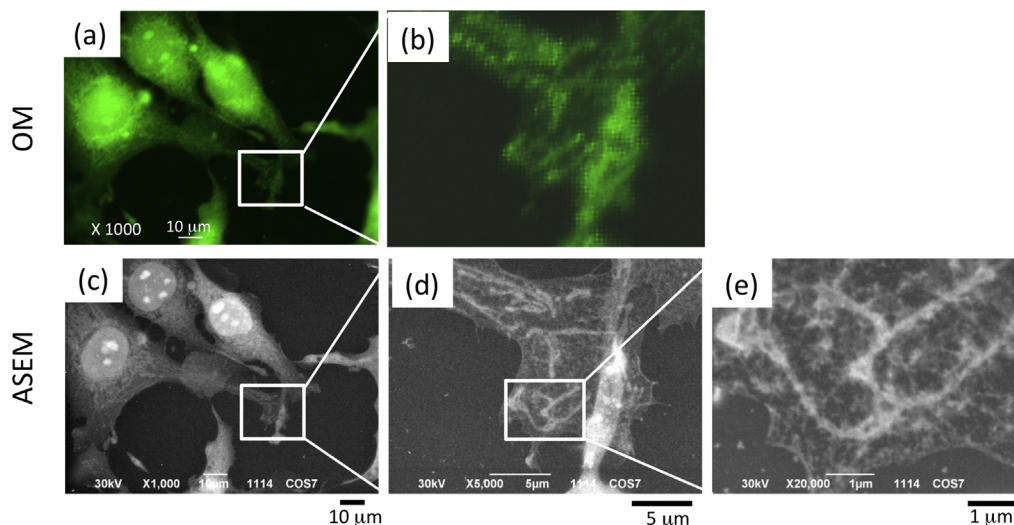
Fig. 22. Endoplasmic reticulum in COS7 cells visualized *ibidem* using (a—b) optical fluorescence microscopy and (c—e) ASEM. The cells were cultured on 100 nm Si_3N_4 film, then fixed with glutaraldehyde [68], perforated, labeled with *anti-protein disulfide isomerase* IgG2b and with Alexa Fluor 488-labeled secondary antibody for OM contrast and, finally further stained with *platinum-blue* for ASEM contrast. The higher magnification images reveal that ASEM offer the far superior resolution.

6. X-ray detection

Electron probes also induce the emission of *characteristic X-rays* from samples. These X-rays are emitted via an electron transitions from an occupied upper level to a lower level where a hole is produced by the irradiation of impacted-electron beam. Therefore, these characteristic X-rays have specific energies for each element present in the sample, which is extremely important for research concerning *nano-materials* [20,99,100]. There are two methods of detecting *characteristic X-rays*: *energy dispersive X-ray spectrometry* (*EDS*) and *wavelength dispersive X-ray spectrometry* (*WDS*). *EDS* is a popular attachment to SEM, because it is easy to use, has a high X-ray detection efficiency and short measurement time.

An *EDS* detector is made by a semiconductor pn junction [20,23,99]. An emitted X-ray photon that enters the detector

Fig. 23. *ECCI* image of a single copper crystal: gauge length = 6 mm, cross section = 4 × 4 mm. The surface-fatigue test was conducted in air. After 1500 cycles of copper fatigue, the surfaces were mechanically and electrolytically polished to produce a planar surface. Landing energy = 15 keV, probe current = 3.5 nA.

hole pairs at the depletion layer of the junction (Fig. 24a). These electrons and holes drift in opposite directions because of the reverse bias applied to the junction, and they are detected by a charge-sensitive pre-amplifier. Their energy is obtained by analyzing the detected charge: the number of electron—hole pairs is determined by the energy of the characteristic X-ray divided by the mean energy of one electron—hole pair generation.

6.1. Progress in SDD

Significant progress in the technology of *EDS* detectors has recently been made in the form of the *silicon drift detector* (*SDD*), which has reduced capacitance and leakage current. The former primarily improves the speed and dynamic range of detection, and the reduction of the leakage current removes the need of liquid-nitrogen cooling.

The energy resolution (FWHM: full width at half maximum) of EDS is described by the following equation:

$$FWHM = 2.35\sqrt{F\varepsilon E + \varepsilon^2(ENC_{el})^2} \qquad (11)$$

where: ENC_{el} = equivalent noise charge attributable to electronic noise; F = fano factor; E = energy of signal X-ray; and ε = energy to excite one electron—hole pair [101]. The values of F and ε are specific to the particular material used to manufacture the semiconductor. ENC_{el} is described as follows [101]:

$$(ENC_{el})^2 = \left(\frac{4kT}{3g_m}C_{tot}^2 A_1\right)\frac{1}{\tau} + \left[\left(2\pi a_f C_{tot}^2\right)A_2\right] + (qI_L A_3)\tau \qquad (12)$$

where C_{tot} = total capacitance of the detector and pre-amplifier; I_L = leakage current of the detector; τ = peaking time or shaping time, which is the time constant that characterizes the shaping amplifier placed after the pre-amplifier; A_1, A_2, and A_3 are constants that are on the order of unity and depend on the shaping algorithm; and a_f is the constant that parameterize the *1/f noise*. The first term is proportional to $1/\tau$ and is related to series noise. The second term is *1/f noise*, and the third term is parallel noise that is proportional to τ [101—104].
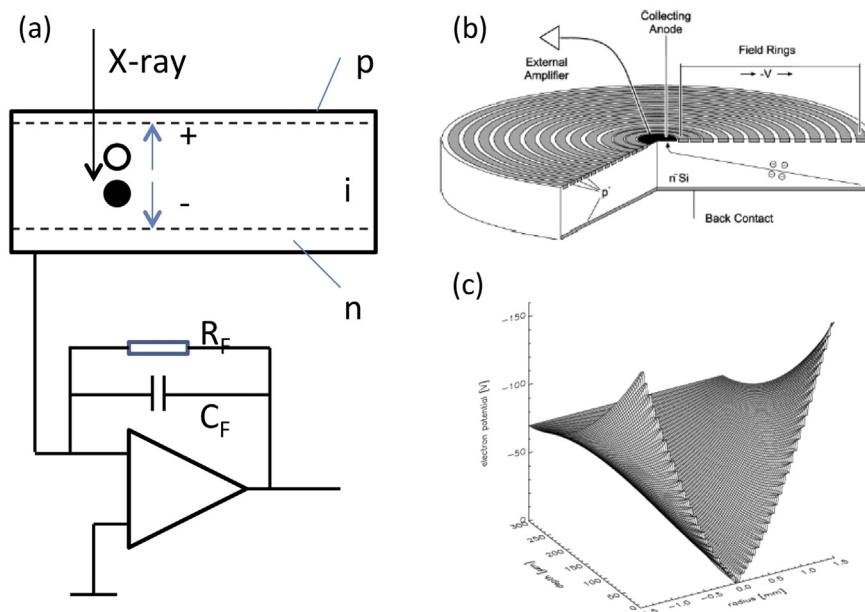
Fig. 24. Structures and potential of X-ray detection devices used for *energy-dispersive spectrometry* (*EDS*). (a) Schematic cross-sectional view of a *traditional EDS device.* (b) Schematic cross-sectional view and (c) potential of a *silicon drift detector* (*SDD*).

Before the development of *SDDs*, pn junctions with a nearly parallel plate shape were most commonly used (Fig. 24a). In such junction, the capacitance between the *p*- and *n*-region proportionally increases with the increase in the X-ray detection area and the increase in the leakage current of the junction caused by thermally excited carriers. This increase in the capacitance enhances the series noise. To reduce this noise, according to equation (12), τ must be long to reduce this noise, limiting the speed of the detection system and degrading the throughput of the X-ray detection. In addition, the contribution of parallel noise, which is affected by the leakage current of the junction associated with thermally excited carriers increases when the shaping time is long. Thus, it is necessary to cool such *pn* junction devises to near liquid-nitrogen temperature [105].

*SDD*s were initially developed in the field of X-ray astronomy and high-energy physics [106]. The *SDD* has been re-designed to be suitable for fluorescent X-ray and characteristic X-ray measurements [105,107,108]. The typical structure of an *SDD* device is shown in Fig. 24b. A p-type region is formed at the X-ray incident surface in an *n*-type silicon substrate. On the opposite side (upper side in Fig. 24b), an *n*-type region near the center and several cylindrically shaped *p*-type regions are formed. Reverse bias is applied between the *p*-type region on the X-ray incident side and the *n*-type region, and reverse biases of higher voltage between the outer *p*-type area and the *n*-type region are applied, thereby permitting the depletion of all regions of the device and leading to the potential distribution shown in Fig. 24c. In this potential distribution, electron potential decreases from the X-ray incident side to the *n*-type region, and it decreases from the outer side to the *n*-type region at the center near the opposite side (upper side in Fig. 24b). As a result, electrons generated by X-rays are collected in the *n*-type region, independent of the location of their generation.

The greatest advantage of *SDD* is *its low capacitance* in comparison with that of traditional *EDS* device. The capacitance of an *SDD* is primarily determined by its structure near the collecting anode (*n*-type region), and it is small because the collecting anode is small in comparison with the parallel-plate-shaped anode of a traditional *EDS* device. Thus, small capacitance is available with a large detection area. A detection area of 150 mm^2 is achievable for *SDDs* [109], while the typical detection area of a traditional *EDS* is 10—30 mm^2. In addition, a small capacitance permits the use of a short shaping time (Equation (12)), which allows the high-speed detection of X-rays, thus improving the throughput of composition analysis [110]. As a result of this fact in combination with the reduction in the leakage current associated with thermally excited carriers caused by the reduced junction area, it is not to operate an *SDD* near liquid-nitrogen, and cooling with a *Peltier-device* is sufficient for good energy resolution [107]. The energy resolution for low-energy X-rays is also improved, because the energy resolution is significantly affected by electronic noise in this region, and it is reduced by the reduction in parallel noise and shot noise attributable to the small capacitance and leakage current, as described above.

Furthermore, *digital pulse processing* (*DSP*) has also been adapted for *EDS* systems. The pulse-shaping method and time affect the energy resolution of *EDS* [102], and these can be optimized using *DSP*. Recent developments of *DSP* methods for *EDS* have been summarized by McCarthy [104].

SDDs offer easy detector maintenance, and provide high-performance *EDS*. In particular, the large detection area of *SDDs* allows the improved composition analysis of *nano-materials*.

6.2. Large area SDD for nano-material analysis

A *BSE* image and *EDS-mapping images* of Au@TiO$_2$ are shown in Fig. 25. In the *BSE* image (Fig. 25a), gold particles can be brightly observed in the TiO$_2$ shells, as described before. In the *EDS-mappin image* shown in Fig. 25b, gold particles are also observed, though not clearly. In this case, the detection area of the *SDD* was 150 mm^2 that corresponds to a solid angle of 0.049 srad. Here, *IE* current was 440 pA, and the substrate voltage was 0 V during the acquisition of the image in Fig. 25b. Because of the large detection area, the detection of faint X-rays from *nano-materials* is possible, thereby permitting the observation of gold nano-particles in *EDS-mapping image*.
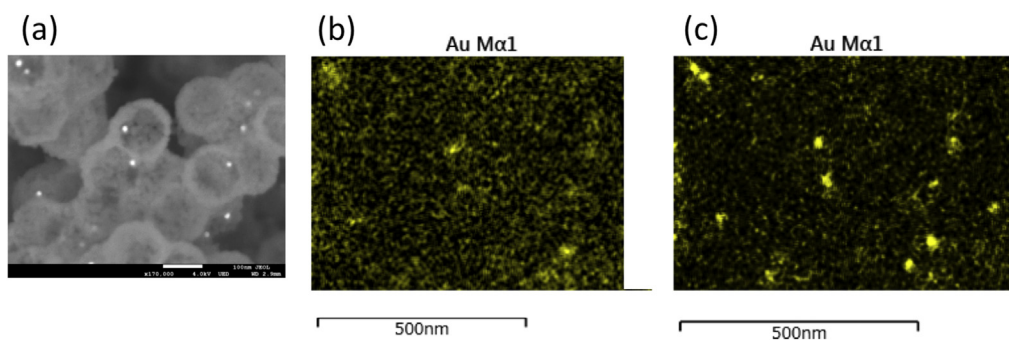
Fig. 25. *BSE image* and *EDS-mapping images* for *Au@TiO₂ yolk-shell materials*. (a) *BSE image*. (b)–(c) *EDS mappings* for Au Mα. An *SDD* detector with a detection area of 150 mm² was used. The probe current was 440 pA, and the acquisition time for the *EDS mapping* was 50 min. The landing energy was 4 keV. The substrate bias was 0 V for (b), and −5 kV for (c).

The performance of the large detection area of an *SDD* can be further improved by applying a substrate bias. In Fig. 25c, an *EDS-mapping image* is shown that was acquired using a device with a detection area of 150 mm² and a substrate bias of −5 kV. The *IE* current was the same as that of Fig. 25b and c. The spatial resolution of *EDS mapping* is usually determined by the beam spreading in a sample, but in this case, it is improved *by the thinning of the IEs* because of substrate bias. At a landing energy of 4 keV, which is relatively low for *EDS* measurements, the combination of large-area *SDD*, and substrate bias permits the composition analysis of *nano-materials* using SEM.

7. Other potential future improvements

7.1. X-ray detection

For very-low-energy X-ray detection, two novel techniques are emerging. One uses a *superconductor* at a very low temperature [111,112], where a superconductor is kept just below its super-conducting transition temperature. An incidence of an X-ray photon increases temperature of the superconductor, which further increases the resistivity of the superconductor. The amount of the resistivity increase is related to the X-ray photon energy. The other uses grating and charge coupled device (CCD), which allow significant increase of detecting X-ray photons for *WDS* [113,114].

7.2. Aberration correction

The use of *multipoles* in TEM has stemmed from proposals [115–117] to significantly improve lens performance through the reduction of third-order spherical aberrations and such devices are now commercially available as *aberration correctors*. In addition, *higher-order aberration correctors* are emerging as a topic of fundamental research [118,119]. Independent research regarding SEM has led to the proposition and fabrication of *second-order chromatic* and *third-order spherical aberration correctors* [120–124], although their utility has yet to be demonstrated in *nano-material* applications.

7.3. Electron source

The development of electron-source *monochromators* has been reported for the purpose of narrowing the energy spread of source electrons, a major contributing factor to chromatic aberration, which itself is a limiting factor for SEM resolution and low landing energies. These efforts offer promising possibilities for the improvement of the resolving-power of low voltage *HRSEM* in the near future [125–127].

8. Conclusions

EM methods play an important role in the characterization of *zeolites, MOFs and related materials* that possess at least one dimension in the nano-scale. These include nano-particles, nano-rods, nano-ribbons, nano-sheets, and nano-films, to name only a few. As the resolution of EM methods improves, more structural detail can be observed in the crystals of *MOFs* and *zeolites*.

The evolution of EM technology, including improvements in the resolution of structural detail, will unquestionably change the traditional characterization of materials, in which only the space average of the crystal lattice is considered by providing the direct and real-time visualization of crystal surfaces and other structures of a few nanometers in thickness.

In short, EM methods are suitable for nano-sized *MOFs* and are able to effectively provide structural details and dynamic information.

References

[1] Liu Z, Fujita N, Miyasaka K, Han L, Stevens SM, Suga M, et al. A review of fine structures of nanoporous materials as evidenced by microscopic methods. Microscopy 2013;62:109–46.

[2] Stevens SM, Jansson K, Xiao C, Asahina S, Klingstedt M, Grüner D, et al. An appraisal of high resolution scanning electron microscopy applied to porous materials. JEOL News 2009;44:17–22.

[3] Holland BT, Blanford CF, Stein A. Synthesis of macroporous minerals with highly ordered three-dimensional arrays of spheroidal voids. Science 1998;281:538–40.

[4] Stein A, Wilson BE, Rudisill SG. Design and functionality of colloidal-crystal-templated materials—chemical applications of inverse opals. Chem Soc Rev 2013;42:2763–803.

[5] Lai C-Z, Fierke MA, Stein A, Bühlmann P. Ion-selective electrodes with three-dimensionally ordered macroporous carbon as the solid contact. Anal Chem 2007;79:4621–6.

[6] Knoll M, Ruska E. Das elektronenmikroskop. Z Phys 1932;78:318–39.

[7] Ruska E. The development of the electron microscope and of electron microscopy. Biosci Rep 1987;7:607–29.

[8] Knoll M. Charging potential and secondary emission of bodies under electron irradiation. Z Tech Phys 1935;16:467–75.

[9] Von Ardenne M. The scanning electron microscope: theoretical fundamentals (in German). Z Physk 1938;109:553–72.

[10] von Ardenne M. The scanning electron microscope: practical construction (in German). Z Tech Phys 1938;19:407–16.

[11] Zworykin VK, Hillier J, Snyder RL. A scanning electron microscope. ASTM Bull 1942;117:15–23.

[12] Oatley CW. The early history of the scanning electron microscope. J Appl Phys 1982;53:R1–13.

[13] Everhart TE. Persistence pays off: Sir Charles Oatley and the scanning electron microscope. J Vac Sci Technol B Microelectron Nanom Struct 1996;14: 3620–4.

[14] Everhart TE, Thornley RFM. Wide-band detector for micro-microampere low-energy electron currents. J Sci Instrum 1960;37:246–8.

[15] Smith KCA. The scanning electron microscope and its fields of application. PhD dissertation. England: Cambridge University; 1956.

[16] Bell DC, Erdman N. Low voltage electron microscopy: principles and applications. John Wiley & Sons; 2012.

[17] Crewe AV, Eggenberger DN, Wall J, Welter LM. Electron gun using a field emission source. Rev Sci Instrum 1968;39:576–83.

[18] Swanson LW, Crouser LC. Angular confinement of field electron and ion emission. J Appl Phys 1969;40:4741–9.

[19] Swanson L, Schwind G. Review of ZrO/W schottky cathode. In: Orloff Jon, editor. Handbook of charged particle optics. 2nd ed. CRC Press; 2008. pp. 1–28.

[20] Goldstein J, Newbury DE, Joy DC, Echlin P, Lyman CE, Lifshin E. Scanning electron microscopy and X-ray microanalysis. USA: Springer; 2003.

[21] Kanaya K, Okayama S. Penetration and energy-loss theory of electrons in solid targets. J Phys Appl Phys 1972;5:43–58.

[22] Seiler H. Secondary electron emission in the scanning electron microscope. J Appl Phys 1983;54:R1–18.

[23] Reimer L. Scanning electron microscopy: physics of image formation and microanalysis. Springer Verlag; 1998.

[24] Drouin D, Hovington P, Gauvin R. CASINO: a new Monte Carlo code in C language for electron beam interactions—part II: tabulated values of the Mott cross section. Scanning 1997;19:20–8.

[25] Dwyer V, Matthew J. A comparison of electron transport in AES/PES with neutron transport theory. Surf Sci 1985;152:884–94.

[26] Sato M. Resolution. In: Orloff Jon, editor. Handbook of charged particle optics. 2nd ed. CRC Press; 2008. pp. 391–435.

[27] Sato M, Orloff J. A method for calculating the current density of charged particle beams and the effect of finite source size and spherical and chromatic aberrations on the focusing characteristics. J Vac Sci Technol B Microelectron Nanom Struct 1991;9:2602–8.

[28] Barth J, Kruit P. Addition of different contributions to the charged particle probe size. Optik 1996;101:101–9.

[29] Joy DC. Contrast in high-resolution scanning electron microscope images. J Microsc 1991;161:343–55.

[30] Joy DC, Joy CS. Low voltage scanning electron microscopy. Micron 1996;27: 247–63.

[31] Reimer L. Image formation in low-voltage scanning electron microscopy. SPIE-International Society for Optical Engineering; 1993.

[32] Drouin D, Couture AR, Joly D, Tastet X, Aimez V, Gauvin R. CASINO V2. 42—a fast and easy-to-use modeling tool for scanning electron microscopy and microanalysis users. Scanning 2007;29:92–101.

[33] Hovington P, Drouin D, Gauvin R. CASINO: a new Monte Carlo code in C language for electron beam interaction—part I: description of the program. Scanning 1997;19:1–14.

[34] Murata K. Spatial distribution of backscattered electrons in the scanning electron microscope and electron microprobe. J Appl Phys 1974;45:4110–7.

[35] Shimizu R, Ikuta T, Everhart T, DeVore W. Experimental and theoretical study of energy dissipation profiles of keV electrons in polymethylmethacrylate. J Appl Phys 1975;46:1581–4.

[36] Joy D, Luo S. An empirical stopping power relationship for low-energy electrons. Scanning 1989;11:176–80.

[37] Cazaux J. Mechanisms of charging in electron spectroscopy. J Electron Spectrosc Relat Phenom 1999;105:155–85.

[38] Ying MH, Thong JTL. Insulator charging under irradiation with a stationary electron probe. Meas Sci Technol 1994;5:1089–95.

[39] Melchinger A, Hofmann S. Dynamic double-layer model – description of time-dependent charging phenomena in insulators under electron-beam irradiation. J Appl Phys 1995;78:6224–32.

[40] Renoud R, Mady F, Ganachaud JP. Monte Carlo simulation of the charge distribution induced by a high-energy electron beam in an insulating target. J Phys-Condens Matter 2002;14:231–47.

[41] Bursill L, Thomas J, Rao K-J. Stability of zeolites under electron irradiation and imaging of heavy cations in silicates. Nature 1981;289:157–9.

[42] Zach J. Resolution limits in low voltage scanning electron microscopes using retarding objective lenses. Nucl Instrum Methods Phys Res Sect A Accel Spectrom Detect Assoc Equip 1990;298:255–9.

[43] Mullerova I, Lenc M. Some approaches to low-voltage scanning electron-microscopy. Ultramicroscopy 1992;41:399–410.

[44] Pease RF. Low voltage scanning electron microscopy. Proc of the 9th Symp on electron, ion and Laser Beam Technology, San Francisco Press, San Francisco; 1967. pp. 176–87.

[45] Yau YW, Pease RFW, Iranmanesh AA, Polasko KJ. Generation and applications of finely focused beams of low-energy electrons. J Vac Sci Technol 1981;19: 1048–52.

[46] Frosien J, Plies E. High performance electron optical column for testing ICs with submicrometer design rules. Microelectron Eng 1987;7:163–72.

[47] Frosien J, Plies E, Anger K. Compound magnetic and electrostatic lenses for low-voltage applications. J Vac Sci Technol B 1989;7:1874–7.

[48] Hordon LS, Huang Z, Maluf N, Browning R, Pease RFW. Limits of low-energy electron optics. J Vac Sci Technol B Microelectron Nanom Struct 1993;11: 2299–303.

[49] Ose Y, Ezumi M, Todokoro H. Improved CD-SEM optics with retarding and boosting electric fields. In: Proceedings of the Society of Photo-optical Instrumentation Engineers (SPIE), metrology, inspection, and process control for microlithography XIII, pts 1 and 21999. p. 930–939.

[50] Yonezawa A, Maruo M, Takeuchi T, Morita S, Noguchi A, Takaoka O, et al. Single pole-piece objective lens with electrostatic bipotential lens for SEM. J Electron Microsc 2002;51:149–56.

[51] Khursheed A. Ultimate resolution limits for scanning electron microscope immersion objective lenses. Optik-Int J Light Electron Opt 2002;113:67–77.

[52] Sato K, Nagoshi M, Kawano T. Application of low-voltage scanning electron microscopy to the characterization of steel surface. Tetsu Hagane-J Iron Steel Inst Jpn 2007;93:99–104.

[53] Todokoro H, Yoneda S, Yamaguchi K, Fukuhara S, Komoda T. Stroboscopic testing of LSIs with low voltage scanning electron microscope. J Microsc 1985;140:313–22.

[54] Nakamae K, Fujioka H, Ura K. A new hemispherical retarding field energy analyser for quantitative voltage measurements in the SEM. J Phys Sci Instrum 1985;18:437.

[55] Cho K, Ryoo R, Asahina S, Xiao C, Klingstedt M, Umemura A, et al. Mesopore generation by organosilane surfactant during LTA zeolite crystallization, investigated by high-resolution SEM and Monte Carlo simulation. Solid State Sci 2011;13:750–6.

[56] Deng H, Grunder S, Cordova KE, Valente C, Furukawa H, Hmadeh M, et al. Large-pore apertures in a series of metal-organic frameworks. Science 2012;336:1018–23.

[57] Liu S, Han L, Duan Y, Asahina S, Terasaki O, Cao Y, et al. Synthesis of chiral TiO_2 nanofibre with electron transition-based optical activity. Nat Commun 2012;3:1215–20.

[58] Kjellman T, Reichhardt NV, Sakeye M, Smått J-H, Lindén M, Alfredsson V. Independent fine-tuning of intrawall-and primary mesoporosity of SBA-15. Chem Mater 2013;25:1989–97.

[59] Galeano C, Güttel R, Paul M, Arnal P, Lu AH, Schüth F. Yolk-Shell gold nanoparticles as model materials for support-effect studies in heterogeneous catalysis: Au,@ C and Au,@ ZrO_2 for CO oxidation as an example. Chem-A Eur J 2011;17:8434–9.

[60] Ogura K, Kersker M. Backscattered electron imaging of GaAs/AlGaAs super lattice structures with an ultra-high-resolution SEM. Proceedings of the 46th Annual Meeting of the Electron Microscopy Society of America; 1988. pp. 204–5.

[61] Ogura K, Ono A, Franchi S, Merli PG, Migliori A. Observation of GaAs/AlAs superlattice structures in both secondary and backscattered electron imaging modes with an ultrahigh resolution scanning electron microscope. Proceedings of the 12th International Congress for Electron Microscopy; 1990. pp. 404–5.

[62] Merli P, Migliori A, Nacucchi M, Govoni D, Mattei G. On the resolution of semiconductor multilayers with a scanning electron microscope. Ultramicroscopy 1995;60:229–39.

[63] Khursheed A. Scanning electron microscope optics and spectrometers. World Scientific; 2011.

[64] Wells OC, Broers A, Bremer C. Method for examining solid specimens with improved resolution in the scanning electron microscope (SEM). Appl Phys Lett 1973;23:353–5.

[65] Merli P, Migliori A, Morandi V, Rosa R. Spatial resolution and energy filtering of backscattered electron images in scanning electron microscopy. Ultramicroscopy 2001;88:139–50.

[66] Green E, Kino G. Atmospheric scanning electron microscopy using silicon nitride thin film windows. J Vac Sci Technol B Microelectron Nanom Struct 1991;9:1557–8.

[67] Thiberge S, Nechushtan A, Sprinzak D, Gileadi O, Behar V, Zik O, et al. Scanning electron microscopy of cells and tissues under fully hydrated conditions. Proc Natl Acad Sci U S A 2004;101:3346–51.

[68] Nishiyama H, Suga M, Ogura T, Maruyama Y, Koizumi M, Mio K, et al. Atmospheric scanning electron microscope observes cells and tissues in open medium through silicon nitride film. J Struct Biol 2010;172:191–202.

[69] Abrams IM, McBrain JW. A closed cell for electron microscopy. J Appl Phys 1944;15:607–9.

[70] Fukushima K, Ishikawa A, Fukami A. Injection of liquid into environmental cell for in situ observations. J Electron Microsc 1985;34:47.

[71] Daulton TL, Little BJ, Lowe K, Jones-Meehan J. In situ environmental cell–transmission electron microscopy study of microbial reduction of chromium(VI) using electron energy loss spectroscopy. Microsc Microanal 2001;7:470–85.

[72] Gai PL. Developments in in situ environmental cell high-resolution electron microscopy and applications to catalysis. Top Catal 2002;21:161–73.

[73] Williamson MJ, Tromp RM, Vereecken PM, Hull R, Ross FM. Dynamic microscopy of nanoscale cluster growth at the solid—liquid interface. Nat Mater 2003;2:532—6.

[74] Creemer JF, Helveg S, Hoveling GH, Ullmann S, Molenbroek AM, Sarro PM, et al. Atomic-scale electron microscopy at ambient pressure. Ultramicroscopy 2008;108:993—8.

[75] Zheng H, Smith RK, Jun YW, Kisielowski C, Dahmen U, Alivisatos AP. Observation of single colloidal platinum nanocrystal growth trajectories. Science 2009;324:1309—12.

[76] de Jonge N, Peckys DB, Kremers GJ, Piston DW. Electron microscopy of whole cells in liquid with nanometer resolution. Proc Natl Acad Sci U S A 2009;106: 2159—64.

[77] Suga M, Nishiyama H, Konyuba Y, Iwamatsu S, Watanabe Y, Yoshiura C, et al. The atmospheric scanning electron microscope with open sample space observes dynamic phenomena in liquid or gas. Ultramicroscopy 2011;111: 1650—8.

[78] Sze SM. VLSI technology. McGraw-Hill; 1998.

[79] Hsu TR. MEMS & microsystems: design, manufacture, and nanoscale engineering. John Wiley & Sons.; 2008.

[80] Harsanyi G. Irregular effect of chloride impurities on migration failure reliability: contradictions or understandable? Microelectron Reliab 1999;39: 1407—11.

[81] Nishiyama H, Teramoto K, Suga M, Sato C. Positively charged nanogold label allows the observation of fine cell filopodia and flagella in solution by atmospheric scanning electron microscopy. Microsc Res Tech 2014;77:153—60.

[82] Sato C, Manaka S, Nakane D, Nishiyama H, Suga M, Nishizaka T, et al. Rapid imaging of mycoplasma in solution using Atmospheric Scanning Electron Microscopy (ASEM). Biochem Biophys Res Commun 2012;417:1213—8.

[83] Murai T, Maruyama Y, Mio K, Nishiyama H, Suga M, Sato C. Low cholesterol triggers membrane microdomain-dependent CD44 shedding and suppresses tumor cell migration. J Biol Chem 2011;286:1999—2007.

[84] Maruyama Y, Ebihara T, Nishiyama H, Suga M, Sato C. Immuno EM-OM correlative microscopy in solution by atmospheric scanning electron microscopy (ASEM). J Struct Biol 2012;180:259—70.

[85] Sugiyama M, Shibata M. Application of scanning electron microscope to dislocation imaging in steel. JEOL News 2011;46:11—6.

[86] Ahmed J, Roberts SG, Wilkinson A. Characterizing dislocation structure evolution during cyclic deformation using electron channelling contrast imaging. Philos Mag 2006;86:4965—81.

[87] Kamaladasa R, Picard Y. Basic principles and application of electron channeling in a scanning electron microscope for dislocation analysis. In: Mexdez-Vilas A, Diaz J, editors. Microscopy: science, technology, applications and education; 2010. pp. 1583—90.

[88] Wilkinson AJ, Hirsch PB. Electron diffraction based techniques in scanning electron microscopy of bulk materials. Micron 1997;28:279—308.

[89] Joy DC. Direct defect imaging in the high resolution SEM. MRS proceedings. Cambridge Univ Press; 1990. pp. 199—209.

[90] Kaneko Y, Hashimoto S. Observation of dislocation structure of fatigued copper single crystals using ECCI method. J-Jpn Inst Metals (In Japanese) 2002;66:1297—303.

[91] Kaneko Y, Hashimoto S. Observation of dislocation structures of fatigued metallic materials by scanning electron microscopy. JEOL News 2003;38:20—3.

[92] Gutierrez-Urrutia I, Zaefferer S, Raabe D. Electron channeling contrast imaging of twins and dislocations in twinning-induced plasticity steels under controlled diffraction conditions in a scanning electron microscope. Script Mater 2009;61:737—40.

[93] Herrera C, Ponge D, Raabe D. Design of a novel Mn-based 1GPa duplex stainless TRIP steel with 60% ductility by a reduction of austenite stability. Acta Mater 2011;59:4653—64.

[94] Gutierrez-Urrutia I, Raabe D. Multistage strain hardening through dislocation substructure and twinning in a high strength and ductile weight-reduced Fe—Mn—Al—C steel. Acta Mater 2012;60:5791—802.

[95] Koyama M, Akiyama E, Tsuzaki K, Raabe D. Hydrogen-assisted failure in a twinning-induced plasticity steel studied under in situ hydrogen charging by electron channeling contrast imaging. Acta Mater 2013;61:4607—18.

[96] Ng B-C, Simkin B, Crimp M. Electron channeling contrast imaging of dislocation structures in deformed stoichiometric NiAl. Mater Sci Eng 1997;239: 150—6.

[97] Wilkinson A, Anstis G, Czernuszka J, Long N, Hirsch P. Electron channelling contrast imaging of interfacial defects in strained silicon-germanium layers on silicon. Philos Mag A 1993;68:59—80.

[98] Kuwano N, Itakura M, Nagatomo Y, Tachibana S. Scanning electron microscope observation of dislocations in semiconductor and metal materials. J Electron Microsc 2010;59:S175—81.

[99] Reed SJB. Electron microprobe analysis. Cambridge, UK: Cambridge University Press; 1997.

[100] Reed SJB. Electron microprobe analysis and scanning electron microscopy in geology. Cambridge: Cambridge University Press; 2005.

[101] Schlosser D, Lechner P, Lutz G, Niculae A, Soltau H, Strüder L, et al. Expanding the detection efficiency of silicon drift detectors. Nucl Instrum Methods Phys Res Sect A Accel Spectrom Detect Assoc Equip 2010;624:270—6.

[102] Gatti E, Manfredi P, Sampietro M, Speziali V. Suboptimal filtering of $1/f$-noise in detector charge measurements. Nucl Instrum Methods Phys Res Sect A Accel Spectrom Detect Assoc Equip 1990;297:467—78.

[103] Bertuccio G, Pullia A, DeGeronimo G. Criteria of choice of the front-end transistor for low-noise preamplification of detector signals at sub-microsecond shaping times for X- and gamma-ray spectroscopy. Nucl Instrum Methods Phys Res Sect A Accel Spectrom Detect Assoc Equip 1996;380: 301—7.

[104] McCarthy J, Friel J, Camus P. Impact of 40 years of technology advances on EDS system performance. Microsc Microanal 2009;15:484—90.

[105] Lechner P, Eckbauer S, Hartmann R, Krisch S, Hauff D, Richter R, et al. Silicon drift detectors for high resolution room temperature X-ray spectroscopy. Nucl Instrum Methods Phys Res Sect A Accel Spectrom Detect Assoc Equip 1996;377:346—51.

[106] Gatti E, Rehak P. Semiconductor drift chamber—an application of a novel charge transport scheme. Nucl Instrum Methods Phys Res 1984;225:608—14.

[107] Fiorini C, Kemmer J, Lechner P, Kromer K, Rohde M, Schulein T. A new detection system for x-ray microanalysis based on a silicon drift detector with Peltier cooling. Rev Sci Instrum 1997;68:2461—5.

[108] Strüder L, Meidinger N, Stotter D, Kemmer J, Lechner P, Leutenegger P, et al. High-resolution X-ray spectroscopy close to room temperature. Microsc Microanal 1998;4:622—31.

[109] Terasaki O, HaeSung C, Minhyung C, Asahina S, Yusuke S, Suga M, et al. Novel structural characterisations of insulating and electron beam sensitive materials employing low voltage high resolution scanning electron microscopy. JEOL News 2013;48:21—31.

[110] Newbury DE. The new X-ray mapping: X-ray spectrum imaging above 100 kHz output count rate with the silicon drift detector. Microsc Microanal 2006;12:26—35.

[111] Irwin K, Hilton G, Wollman D, Martinis JM. X-ray detection using a superconducting transition-edge sensor microcalorimeter with electrothermal feedback. Appl Phys Lett 1996;69:1945—7.

[112] Tanaka K, Nagata A, Sasayama N, Ikeda M, Odawara A, Nakayama S, et al. High-Energy resolution microcalorimeter EDS system for electron beam excitation. J Surf Anal 2005;12:122.

[113] Terauchi M, Koike M, Fukushima K, Kimura A. Development of wavelength-dispersive soft X-ray emission spectrometers for transmission electron microscopes—an introduction of valence electron spectroscopy for transmission electron microscopy. J Electron Microsc 2010;59:251—61.

[114] Takahashi H, Handa N, Murano T, Terauchi M, Koike M, Kawachi T, et al. A soft X-ray emission spectrometer with high-energy resolution for electron probe microanalysis. J Electron Microsc 2010;16:34—5.

[115] Rose H. Outline of a spherically corrected semiaplanatic medium-voltage transmission electron microscope. Optik 1990;85:19—24.

[116] Haider M, Braunshausen G, Schwan E. Correction of the spherical aberration of a 200 kV TEM by means of a Hexapole-corrector. Optik 1995;99:167—79.

[117] Krivanek OL, Dellby N, Lupini AR. Towards sub-electron beams. Ultramicroscopy 1999;78:1—11.

[118] Sawada H, Sasaki T, Hosokawa F, Yuasa S, Terao M, Kawazoe M, et al. Correction of higher order geometrical aberration by triple 3-fold astigmatism field. J Electron Microsc 2009;58:341—7.

[119] Krivanek OL, Nellist PD, Dellby N, Murfitt MF, Szilagyi Z. Towards sub-0.5 electron beams. Ultramicroscopy 2003;96:229—37.

[120] Zach J, Haider M. Aberration correction in a low voltage SEM by a multipole corrector. Nucl Instrum Methods Phys Res Sect A Accel Spectrom Detect Assoc Equip 1995;363:316—25.

[121] Honda K, Takashima S. Chromatic and spherical aberration correction in the LSI inspection scanning electron microscope. JEOL News 2003;38:36—40.

[122] Uno S, Honda K, Nakamura N, Matsuya M, Zach J. Aberration correction and its automatic control in scanning electron microscopes. Optik-Int J Light Electron Opt 2005;116:438—48.

[123] Kazumori H, Honda K, Matsuya M, Date M, Nielsen C. Field emission SEM with a spherical and chromatic aberration corrector. Microsc Microanal 2004;10:1370—1.

[124] Kawasaki T, Nakano T, Hirose K. Developing an aberration-corrected Schottky emission SEM and method for measuring aberration. Microelectron Eng 2009;86:1017—20.

[125] Mackie WA, Morrissey JL, Hinrichs CH, Davis PR. Field emission from hafnium carbide. J Vac Sci Technol Vac Surf Film 1992;10:2852—6.

[126] Zhang H, Tang J, Yuan J, Ma J, Shinya N, Nakajima K, et al. Nanostructured LaB6 field emitter with lowest apical work function. Nano Lett 2010;10: 3539—44.

[127] Mukai M, Inami W, Omoto K, Kaneyama T, Tomita T, Tsuno K, et al. Monochromator for a 200 kV Analytical electron microscope. Microsc Microanal 2006;12:1206—7.